

Hydrodynamic and N-body Schemes On An Unstructured, Adaptive Mesh with Applications to Cosmological Simulations

Guohong Xu

Board of Studies in Astronomy and Astrophysics,

University of California at Santa Cruz,

Santa Cruz, California 95064

em ail: xu@ucolick.org

Submitted at October 1, 2021, Revised at.....

ABSTRACT

The theory and application of numerical methods for unstructured meshes have been improved significantly in recent years. Because the grids can be placed arbitrarily in space, unstructured meshes can provide much higher spatial resolution than regular meshes. The built-in nature of mesh adaptivity for unstructured meshes gives one way to simulate highly dynamic, hierarchical problems involving both collisionless dark matter and collisional gas dynamics. In this paper, we describe algorithms to construct unstructured meshes from a set of points with periodic boundary conditions through Delaunay triangulation, and algorithms to solve hydrodynamic and N-body problems on an unstructured mesh. A combination of a local transformation algorithm and the traditional Bowyer-Watson algorithm gives an efficient approach to perform Delaunay triangulation. A novel algorithm to solve N-body equations of motion on an unstructured mesh is described. Poisson's equation is solved using the conjugate gradient method. A gas-kinetic scheme based on the BGK model to solve Euler equations is used to evolve the hydrodynamic equations. We apply these algorithms to solve cosmological settings, which involve both dark and baryonic matter. Various cooling and heating processes for primordial baryonic matter are included in the code. The numerical results show that the N-body and hydrodynamic algorithms based on unstructured meshes with mesh refinement are well-suited for hierarchical structure formation problems.

subject headings numerical methods, cosmology, galaxy formation.

1. Introduction

Numerical simulations in astrophysics turn out to be very challenging because of the large dynamical range required in three dimensions. Examples include modeling of star

forming regions and the origin of galaxies. In cosmology, structures are believed to have formed hierarchically, requiring a simultaneous modeling of structures on scales of ~ 100 Mpc and ~ 10 kpc. Various hydrodynamical techniques have been explored to achieve such a large dynamic range, from Eulerian methods using regular meshes (c.f. Cen 1992 and Ryu et al. 1993) and recently with Adaptive Mesh Refinement (AMR, c.f. Berger & Colella 1989, Klein, Colella, & McKee 1992) to Lagrangian methods like Smoothed Particle Hydrodynamics (SPH, c.f. Hemquist & Katz 1989, Katz, Weinberg, & Hemquist 1996). Eulerian schemes without AMR are inadequate because of computational expense and are wasteful because high resolution is typically not required at all points in a simulation volume. SPH methods provide higher spatial resolution than regular mesh Eulerian methods such as TVD and PPM, but have poorer shock resolution than shock capturing methods.

N-body codes can be classified as direct, in the case of Particle-Particle methods and TREE methods (Barnes & Hut 1986, Hemquist 1987), or grid-based, such as the Particle-Mesh method (Efsthathiou et al. 1985), or hybrids, such as P³M (Hockney & Eastwood 1981) or TPM (Xu 1995), depending on the potential solver. In cosmological simulations involving gas and dark matter it is desirable that the N-body and hydro solvers achieve similar spatial resolution. Normally, Eulerian schemes for N-body and gas are combined, such as PM+TVD code (Ryu et al. 1993), and Lagrangian schemes go together, such as TREESPH (Hemquist & Katz 1989). Numerically it is appreciate to employ similar algorithms for N-body and gas dynamics.

Recently, unstructured meshes have become increasingly popular in many fields, such as geophysics, seismology, structural mechanics and computational fluid dynamics. When combined with an accurate shock-capturing technique, codes employing unstructured meshes have many advantages over particle based algorithms and Eulerian codes with regular grids, in principle. In an unstructured mesh, grid points are connected by triangles in two dimensions and tetrahedra in three dimensions. Since grid points can be placed arbitrarily, an optimal mesh can be configured for any applications. Mesh refinement can be achieved by simply adding more grid points and reconnecting the mesh. The refined mesh will have the same topology as the original one except that it will have more cells, thus mesh refinement adds no overhead to algorithms designed for unstructured meshes. Although the nodes in an unstructured mesh can be irregularly distributed, the internal data structure used to represent the grid is homogeneous as opposed to block-structured grids where block boundaries and interiors must be distinguished. As described below, only local grid operations are needed to solve equations on unstructured meshes, hence the codes can be easily parallelized.

In this paper, we describe techniques to construct unstructured meshes and algorithms

to solve N-body and gas dynamic problems on these grids. We apply this code to perform cosmological N-body + hydrodynamic simulations, including various cooling and heating processes and mesh refinement. To avoid lengthy mathematical derivations of the algorithms, we put all the required formulas in the appendices.

2. Numerical Algorithms on Unstructured Meshes

2.1. Construction of Unstructured Meshes

Unstructured meshes are constructed from arbitrarily scattered points in n -dimensional space by Delaunay triangulation. The mathematical definition of Delaunay triangulation can be found in text books on geometric design. An example of Delaunay triangulation in 2-dimensional space is illustrated in Figure 1. The scattered points are connected by non-overlapping triangles obeying certain rules. The interior of the circum circle of any triangle contains no other point in the point set. Delaunay triangulation is unique provided that no $n + 2$ points are co-spherical in n -dimensional space. There are many properties associated with Delaunay triangulation (c.f. Lawson 1986, Barth 1995), many of which will be cited in our paper without strict mathematical description. In Appendix A, we gave the essential formulas for geometric relations between a point and a simplex (triangle in 2D and tetrahedron in 3D).

Much effort has been devoted to designing algorithms to perform Delaunay triangulation. Among these, incremental insertion algorithms are of particular interest, since we will incorporate mesh refinement to enhance resolution. The methods of Bowyer (Bowyer 1981) and Watson (Watson 1981) are very similar. When a new point is inserted into the existing triangulation, those simplices with their circum spheres enclosing the new point are deleted and new simplices corresponding to those just deleted are added. The Bowyer-Watson algorithm is straight-forward to implement and is efficient ($O(N^{1+1/n})$ in n -dimensional space). Another triangulation method is the edge swapping algorithm of Green and Sibson (Green & Sibson 1977), which was extended to 3D by Joe (Joe 1989). Edge swapping algorithms insert a new point into the simplex that encloses it, and perform a sequence of local transformations until no further local transformations can be performed. The edge swapping algorithm is slightly slower (also $O(N^{1+1/n})$), but can be adopted to handle different criteria to perform local transformations.

For cosmological simulations, we require a triangulation algorithm for a set of points in a periodic box. The Bowyer-Watson algorithm appears to have difficulties with periodic boundaries when the number of points in the box is small, because some triangles might

have two vertices that are periodic images of the same point. The edge swapping algorithm, however, can be applied to periodic volumes. Thus a combined Bowyer-Watson algorithm with edge swapping algorithm is efficient for periodic boxes. In Figure 2 we show an example of a 2-dimensional unstructured mesh for 1000 random points in a periodic box.

Our data structures to describe the geometric connections in an unstructured mesh differ from those used previously (e.g. Kallinderis & Vijayan 1993). Two data types represent an unstructured mesh: nodes and cells. A node contains a vector to describe the position of a point and a flag to record the refinement level. A cell contains $n + 1$ pointers to its vertices, another $n + 1$ pointer to its neighbor simplices, and an integer flag to record various information about the cell's status and its relation to its neighbors. With periodic boundaries, another two integer flags record the relative position between the simplex and its vertices and its neighbor simplices. So the memory requirement with periodic boundaries is $n + 1$ words for each node and $2n + 5$ words for each cell. This implies that the total memory required to store an unstructured mesh is about $3 + 2 \times 9 = 21$ words per node in 2-D, and $4 + 6 \times 11 = 70$ words per node in 3-D.

2.2. N-body algorithms on unstructured meshes

Gravitational accelerations in N-body systems can be calculated either from particle-particle methods or particle-mesh techniques. Below we introduce a new particle-mesh algorithm for unstructured grids.

The discretized Poisson's equation on an unstructured mesh can be derived as follows. Consider node 0 as illustrated in Figure 3. We choose the control volume for node 0 with the boundary connected by the middle points of the edges and middle point of each simplex associated with node 0, such as that indicated by the dotted lines in Figure 3. Integrating Poisson's equations over this control volume gives,

$$\int_V \nabla^2 \phi = \int_V \frac{\rho}{\rho_0} = \frac{M_0}{V_0}; \quad (1)$$

where V_0 and M_0 are the control volume and mass of node 0, respectively. If we linearly interpolate the potential field in each simplex T_i , we have $\phi(\mathbf{x}) = \sum_k w_k(\mathbf{x}) \phi_k$, where $w_k(\mathbf{x})$ is the weighting to vertex k . It can be shown that $w_k(\mathbf{x})$ is equal to the barycentric coordinates of a point located at \mathbf{x} relative to vertex k of simplex T_i (see Appendix A for more details). Using Gauss' theorem, the left hand side of equation (1) can be written as,

$$\int_V \nabla^2 \phi = \oint_{\partial V} \nabla \phi \cdot \mathbf{n} = \sum_{T_i} \int_{T_i} \nabla^2 \phi = \sum_{T_i} \frac{V_i}{n} \sum_{k=0}^n \nabla^2 \phi_k w_k(\mathbf{x})_k; \quad (2)$$

where V_i is the volume of simplex T_i and n is the dimension of space. This result is the same as that derived using the Galerkin finite element approximation (Barth 1995).

The discrete Poisson's equation resulting from this procedure is a system of linear equations, $M_{ij} \phi_j = b_i$, where M_{ij} is a symmetric sparse matrix. Since the matrix M is sparse, the conjugate gradient method can be used to solve this linear system efficiently. To guarantee convergence, we require that M be positive definite. A necessary and sufficient condition for M to be positive definite is that the triangulation is a Delaunay triangulation (Barth 1995). The convergence rate of this simple conjugate gradient method is shown in Figure 4. The error decreases exponentially with the number of iterations, given a good initial guess of the potential. In N -body simulations, we can always use the solution in the previous step as the initial guess. Our numerical experiments indicate that the number of iterations required to achieve convergence during the next time step is typically about 20–50.

In order to solve Poisson's equation on an unstructured mesh for N -body problem, we must interpolate particles to the mesh. For regular mesh, particle interpolation can be done using the Cloud-in-Cell (CIC) interpolation (see, for example Efsthliou et al. 1985). For an unstructured mesh, a similar procedure can be used. For each particle, we identify the cell containing the particle, and calculate the barycentric coordinate b_i of the particle inside the cell according to equation (A2). Mass is assigned to each node of the tetrahedral cell with weighing factor b_i . After particle mass interpolation, the density of each node obtained by dividing its mass by its dual volume.

After solving for the gravitational potential, the acceleration on each node is calculated from the average of its control volume. For example, the acceleration at node 0 in Figure 3 is,

$$\vec{F}_0 = \frac{1}{V_0} \int_{T_i} (\nabla \phi) dV = \sum_{T_i} \frac{V_i}{V_0} \sum_{k=0}^{X^n} a_k \vec{r}_k : \quad (3)$$

The acceleration on each particle is calculated in a similar fashion as in the Particle-Mesh algorithm,

$$\vec{F}_i = \sum_{k=0}^{X^n} w_k(\vec{x}_i) \vec{F}_k : \quad (4)$$

The above formulation, when applied to a regular mesh, is identical to the Particle-Mesh algorithm with CIC interpolation.

In Figure 5, we show the force between two equal mass particles with different separations and orientation obtained using the above algorithm. The force behaves similarly to the PM method, i.e. accurate long distance forces, but underestimate short range force. The force is not very noisy within one cell, which indicates the force resolution can be

improved using techniques similar to P^3M . The force resolution is roughly 1.5×2 cells, which is slightly better than the PM algorithm because each node is connected with more cells in an unstructured mesh than in a regular mesh. The deviation from r^{-2} -law at large separations is due to periodic boundaries.

As discussed later, mesh refinement can be performed at low cost, so we can achieve high spatial resolution using unstructured meshes for the N-body problem.

2.3. Hydrodynamics on unstructured meshes

The Euler equations are solved on unstructured meshes through the Finite Volume scheme (c.f. Vijayan & Kallinderis 1994),

$$\sum_V \frac{\partial U}{\partial t} dV + \sum_e F(U) \cdot \mathbf{e} = 0; \quad (5)$$

where $U = f; \mathbf{v}; E g^T$ represents the fluid state and $F(U)$ is the flux vector. Before we write down the discrete form of the equations, we need to decide whether we want to store the fluid variables on the nodes or in the cells. The node representation uses less memory because the number of cells is typically 5–6 times the number of nodes in 3-D. But there are indications that the cell representation gives higher resolution than node representation (see Mavriplis 1992 for a discussion). We choose node representation to minimize memory usage. Consider node 0 in Figure 3 with its control volume illustrated in the figure. We have,

$$\frac{\partial U}{\partial t} \Big|_0 = \frac{1}{V_0} \sum_{k \in N_i} F_{0k} \cdot S_{0k}; \quad (6)$$

where N_i is the set of neighboring vertices connected with node 0, F_{0k} is the flux at the middle of edge $0-k$, and S_{0k} is the total surface area of the control volume related to edge $0-k$. All we need is a method to calculate the flux in the middle of each edge accurately.

Previous approaches to solve the Euler equations have used Upwind schemes of various types to calculate the flux at the edges (c.f. Barth 1995). Upwind schemes require artificial viscosity to achieve better than first order accuracy. Here we introduce a new approach based on the gas kinetic theory of fluid dynamics.

The hydrodynamic equations (both the Euler equations and the Navier-Stokes equations) can be derived from Boltzmann's equation through the Chapman-Enskog procedure (see, for example, Shu 1991, Chapters 2 & 3). It is quite physical to derive numerical schemes for hydrodynamic equations using the gas-kinetic theory. Recently, Xu

& Prendergast (1994) and Xu, Martinelli, & Jameson (1995) successfully developed such numerical schemes based on the BGK model (Bhatnagar, Gross, & Krook 1954) of the collisional Boltzmann's equation,

$$\frac{\partial f}{\partial t} + \mathbf{u} \cdot \nabla_{\mathbf{x}} f = \frac{g - f}{\tau}; \quad (7)$$

where $g(\mathbf{t}; \mathbf{x}; \mathbf{u})$ is the equilibrium distribution function and τ is the collisional time scale. The BGK model accurately describes a large range of situations, from very high density, high temperature flows to very high Mach number ($> 10^4$) flows. The solution to this equation can be written as

$$f(\mathbf{t}; \mathbf{x}; \mathbf{u}) = \frac{1}{\tau} \int_0^{\mathbf{t}} g(\mathbf{t}^0; \mathbf{x}^0; \mathbf{u}) e^{-(\mathbf{t}-\mathbf{t}^0)/\tau} d\mathbf{t}^0 + e^{-(\mathbf{t}-\mathbf{t}^0)/\tau} f_0(\mathbf{x} - \mathbf{u}(\mathbf{t}-\mathbf{t}^0); \mathbf{u}) \quad (8)$$

where $\mathbf{x}^0 = \mathbf{x} - \mathbf{u}(\mathbf{t} - \mathbf{t}^0)$ and $f_0(\mathbf{x}; \mathbf{u})$ is the initial state.

The macroscopic quantities $U(\mathbf{t}; \mathbf{x})$ and $\mathbf{F}(\mathbf{t}; \mathbf{x})$ are moments of the distribution function $f(\mathbf{t}; \mathbf{x}; \mathbf{u})$,

$$U = \int \mathbf{u} f d\mathbf{u} d\mathbf{x} \quad (9)$$

$$\mathbf{F} = \int \mathbf{u} \mathbf{u} f d\mathbf{u} d\mathbf{x} \quad (10)$$

where,

$$f = \frac{1}{\tau} \int_0^{\mathbf{t}} \frac{1}{\tau} \int \mathbf{u} \mathbf{u} f d\mathbf{u} d\mathbf{x} d\mathbf{t}^0 + e^{-(\mathbf{t}-\mathbf{t}^0)/\tau} f_0(\mathbf{x} - \mathbf{u}(\mathbf{t}-\mathbf{t}^0); \mathbf{u}) \quad (11)$$

with \mathbf{u} representing the internal variable with K degrees of freedom which will be discussed in Appendix B.

Consider an edge which connects two nodes. Without loss of generality, we assume that the two ends of the edge have coordinates $(\mathbf{x}_1=2;0;0)$ and $(\mathbf{x}_2=2;0;0)$, and that the current time is $\mathbf{t} = 0$ and the time step is $\Delta \mathbf{t}$. the current position in consideration is $\mathbf{x} = 0$. Following the treatment in Xu, Martinelli, & Jameson (1995), we can expand the distributions f_0 and g along the x -direction around the edge center as follows,

$$f_0(\mathbf{x}; \mathbf{u}) = \begin{cases} g_0^L(1 + A^L \mathbf{x}); & \mathbf{x} < 0 \\ g_0^R(1 + A^R \mathbf{x}); & \mathbf{x} > 0 \end{cases} \quad (12)$$

$$g(\mathbf{t}; \mathbf{x}; \mathbf{u}) = g_0^G \begin{cases} 1 + A^{GR} \mathbf{x} + B \mathbf{t}; & \mathbf{x} < 0 \\ 1 + A^{GL} \mathbf{x} + B \mathbf{t}; & \mathbf{x} > 0 \end{cases} \quad (13)$$

Here g_0 is the equilibrium state, which is a Boltzmann distribution for hydrodynamic equations. The coefficients of $A^L; A^R; A^{GL}; A^{GR}; B$ can be expanded in velocity space

as $A^L = A^L$, $A^R = A^R$, $A^{GL} = A^{GL}$, $A^{GR} = A^{GR}$, $B = B$, with $A^L; A^R; A^{GL}; A^{GR}; B$ being constants. The reason for the splitting of the right hand side and the left hand side has its physical basis (Xu, Martinelli, & Jameson 1995) and serves as the mechanism for shock capturing in the scheme.

Substituting the solutions to equation (8) after the integration, we get,

$$f(t; 0; u) = (1 - e^{t^*})g_0^{L=R} + (1 + (t + t^*)e^{t^*})u_x A^G g_0^{L=R} + (t + t^* + e^{t^*})B g_0^{L=R} + e^{t^*} f_0(t; u): \quad (14)$$

This distribution is used to calculate the flux function $F(t; x)$ through moment integration (equation 10).

Notice in the above derivation that it does not matter if the gas is 1-D or 3-D. In this sense, the BGK gaskinetic scheme is truly multiple dimensional without involving vector splitting which are usually used in TVD or PPM codes to generalize from 1-D space to multiple dimensional space.

3. Cosmological Equations

The dynamical equations for dark matter and gas in a comoving frame can be written as follows (c.f. Peebles 1980, Cen 1992),

$$\frac{d\mathbf{x}_i}{dt} = \frac{1}{a}\mathbf{v}_i \quad (15)$$

$$\frac{d\mathbf{v}_i}{dt} + \frac{\mathbf{a}}{a}\mathbf{v}_i = -\frac{1}{a}\mathbf{r} \quad (16)$$

$$r^2 = \frac{4}{a}G(\rho_0) \quad (17)$$

$$\frac{\partial}{\partial t} + \frac{1}{a}\frac{\partial}{\partial \mathbf{x}_k}v_k = 0 \quad (18)$$

$$\frac{\partial v_j}{\partial t} + \frac{1}{a}\frac{\partial}{\partial t}v_j v_k + \frac{1}{a}\frac{\partial p}{\partial \mathbf{x}_j} = -\frac{a}{a}v_j - \frac{1}{a}\frac{\partial}{\partial \mathbf{x}_j} \quad (19)$$

$$\frac{\partial E}{\partial t} + \frac{1}{a}\frac{\partial (E + P)}{\partial \mathbf{x}_k}v_k = -2\frac{a}{a}E - \frac{1}{a}\mathbf{v} \cdot \mathbf{r} + H \quad (20)$$

The polytropic equation of state is normally adopted for an adiabatic gas,

$$E = \frac{1}{2}v^2 + \frac{p}{\gamma - 1}: \quad (21)$$

These equations can be simplified by defining, $dt^0 = a^2 dt$, $v_k^0 = av_k$, $E^0 = a^2 E$, $p^0 = a^2 p$ and $\rho^0 = a^2 \rho$, yielding,

$$\frac{\partial}{\partial t^0} + \frac{\partial v_k^0}{\partial x_k} = 0; \quad (22)$$

$$\frac{\partial v_j^0}{\partial t^0} + \frac{\partial v_j^0 v_k^0}{\partial x_k} + \frac{\partial p^0}{\partial x_j} = - \frac{\partial E^0}{\partial x_j}; \quad (23)$$

$$\frac{\partial E^0}{\partial t^0} + \frac{\partial (E^0 + p^0) v_k^0}{\partial x_k} = - v_k^0 \frac{\partial E^0}{\partial x_k} + a^4 (H^0); \quad (24)$$

$$E^0 = \frac{1}{2} v^2 + \frac{p^0}{\rho^0}; \quad (25)$$

3.1. Time Integration Scheme

The equations of motion for the dark matter are integrated using a time-centered, second order accurate leapfrog algorithm. The particle positions are one half time step ahead of their velocities.

$$\mathbf{x}_i^{n+1/2} = \mathbf{x}_i^{n-1/2} + a^1 \mathbf{v}_i^n \Delta t; \quad (26)$$

$$\mathbf{v}_i^{n+1} = \frac{1 - \frac{1}{2} H(t) \Delta t}{1 + \frac{1}{2} H(t) \Delta t} \mathbf{v}_i^n + a^1 \mathbf{F}_i^{n+1/2} \frac{\Delta t}{1 + \frac{1}{2} H(t) \Delta t}; \quad (27)$$

where $\mathbf{F} = -\nabla \Phi$.

In applying mesh refinement, we allow the system time step based on gravity to adjust according to,

$$\Delta t_{\text{grav}} = c_{\text{grav}} \min_{i,j} \frac{v_{\text{esc}}}{\max(\mathbf{F}_i, \mathbf{F}_j)}; \quad (28)$$

where l_{ij} is the length of the edge between nodes i and j in the unstructured mesh, and \mathbf{F}_i is the gravitational acceleration at node i . The constant c_{grav} has a meaning similar to the CFL condition in hydrodynamics. Our numerical experiments show that $c_{\text{grav}} = 0.3$ is a good choice.

When the time step changes from Δt_1 to Δt_2 , we adjust the particles positions from $t + \Delta t_1/2$ to $t + \Delta t_2/2$ using the following second order accurate formula,

$$\mathbf{x}_i(t + \Delta t_2/2) = \mathbf{x}_i(t + \Delta t_1/2) + \frac{(\Delta t_2 - \Delta t_1)}{2} \mathbf{v}_i(t) + \frac{(\Delta t_2^2 - \Delta t_1^2)}{8} \mathbf{a}_i(t + \Delta t_1/2); \quad (29)$$

The Courant-Friedrichs-Lewy (CFL) stability criterion determines the hydrodynamic time step for the system. We use simplified version of the CFL criterion in an unstructured

{ 10 {

mesh,

$$t_{\text{hydro}} < \min_{ij} \frac{l_{ij}}{\max_{k=i,j} (v_k n_{ij} + c_{s,k})} ; \quad (30)$$

where l_{ij} is the length of edge $i-j$, n_{ij} is the unit vector indicating the edge direction and c_s is the sound speed. We argue that the above criterion is sufficient to satisfy the CFL stability criterion described in Barth (1995).

The gravitational terms in the cosmological hydrodynamic equations can be solved consistently in the gas kinetic scheme by including the force term in Boltzmann's equation. But it would be rather expensive to do so. Instead, we treat these terms as source terms due to an external force. The fluxes due to gravitational acceleration are calculated as follows,

$$G = 0; \quad (31)$$

$$G \cdot \mathbf{v}^0 = \frac{1}{2} (\mathbf{v}^{(n+1)} + \mathbf{v}^{(n)}) \mathbf{F}^{0(n+1=2)} \cdot \mathbf{t}; \quad (32)$$

$$G \cdot \mathbf{E}^0 = \frac{1}{2} (\mathbf{v}^{0(n+1)} + \mathbf{v}^{0(n)}) \mathbf{F}^{0(n+1=2)} \cdot \mathbf{t}; \quad (33)$$

where $\mathbf{F}^0 = \mathbf{r}^0$. Since the hydrodynamic quantities are synchronized with the velocity field of the dark matter, when the system time step changes, we still need only to change the particle positions. For the hydrodynamic time step, we allow for variable CFL constant from one time step to another in order to limit the change of system time step.

3.2. Radiative Cooling

Various cooling and heating processes relevant to primordial gas have been included in the code (see Appendix D for a list of processes). Since the cooling time can be very short compare with hydrodynamic time (c.f. Figure 6), we have to be very careful with time integration of the energy equation when cooling processes are turned on. In our implementation, we integrated the cooling function with adjustable time steps within one system time step. The variable step, fifth order accurate Runge-Kutta integrator described in Press et al. (1992) is used to integrate the following equation,

$$\frac{du}{dt} = \frac{u}{t} + H ; \quad (34)$$

where u is the thermal energy, \dot{u} is the thermal energy change due to gravity and hydrodynamics, t is the system time step and Λ is the cooling function. This equation is integrated from 0 to t using many time steps depending on the cooling time scale. Our numerical experiments show that sometimes about 10^4 time steps is required within one dynamical time step t .

3.3. Mesh Refinement Algorithms

For an unstructured mesh, cells can be refined arbitrarily. Vijayan & Kallinderis (1994) discuss strategies for cell division. One can put a node in the center of an edge, in the middle of a face, in the middle of a cell, or a combination of all of them.

In cosmological simulations, we want to resolve forming structures. For N -body problems, we use a mass criteria m_c to determine mesh refinement. After we interpolate particle data to mesh nodes, each node carries a mass. For each face of a cell in the unstructured mesh, we put a refining node at the center of the face if the linearly interpolated mass at the center is above m_c .

For hydrodynamic problems, following the criteria for galaxy formation in (Cen & Ostriker 1993), we put a refining node in the middle of a cell if the gas in this cell, (a) is contracting, $\nabla \cdot \mathbf{v} < 0$, and (b) has a mass greater than the Jean's mass, $m_b > m_J$. When cooling processes are included we also require the cooling time to be shorter than the dynamical time, $t_{\text{cool}} < t_{\text{dyn}}$.

4. Code Tests and Performance

4.1. Testing 1D gas-kinetic scheme

In Figure 7, we show the results of a Lax shock tube test. The initial conditions for this test is $U = (0.445; 0.311; 8.928)$ for $x < 0$ and $U = (0.5; 0; 1.4275)$ for $x > 0$. The result is at $t = 0.15$. The contact discontinuity is resolved with about 2 cells, the rarefaction shock was sharply captured with about two cells and no post-shock oscillation is observed.

One test that is closely related to structure formation in cosmology is described in Ryu et al. (1993) with the following initial conditions: $\rho = 0$, $v(x) = \sin(2\pi x)/2$, $p = 10^4$, and periodic boundary condition for $0 \leq x < 1$. Our results at $t = 3$ are presented in Figure 8. We notice that the BGK gas-kinetic scheme can successfully resolve features within two cells without any artificial viscosity or adjustment for the temperature term due to high Mach number. Our scheme successfully reproduces the density caustic, the saw-shape velocity field, and segmented pressure field with small oscillation. The Mach number involved in this test is much higher ($\sim 10^4$) than that in usual shock tube tests. This result demonstrates that the BGK gas-kinetic scheme is very robust in high Mach number situations.

4.2. Cosmological N-body Simulations

We construct the initial conditions for the Cold Dark Matter model using the Zel'dovich approximation (cf. Efstathiou et al. 1985). Initially, particles are almost uniformly distributed. As the system evolves, structure forms due to gravitational clustering. More and more massive objects form as time passes by. We show our results with a 32^3 uniform mesh in Figure 9, and results with mesh refinement from a 32^3 uniform mesh in Figure 10. The final mesh nodes are shown in Figure 11, which indicates that our mesh refinement traces the particle distribution very well. Here, the mesh refinement is performed on the faces of tetrahedra. A new node is put in the middle of a face if the mass on all the three nodes are above a certain value. In this test case, the critical mass is taken to be $5m_i$, where m_i is the mass for each particle. Visually, we can already see the great improvement of the resolution with mesh refinement. The two-body correlation function $\xi(r)$ (see Peebles 1980 for a definition) for two simulations with and without mesh refinement is shown in Figure 12. The resolution improvement of the simulation with mesh refinement over the simulation without mesh refinement is well above a factor of 10, while the running time between the two simulations for each time step is less than a factor of two.

4.3. Cosmological N-body + Gas Simulations

Recently Frenk et al. (1996) have proposed a comparison between different cosmological hydrodynamic codes. They set up a constrained initial conditions for a CDM model. The initial conditions for the results described below are generated from their density field using the Zel'dovich approximation (Efstathiou et al. 1985). Readers can compare some of our results to others presented in their paper (Frenk et al. 1996) with the same initial conditions. All the tests shown below are obtained with 32^3 particles and 32^3 raw mesh with mesh refinement.

In Figure 13, we show the density and temperature contours of a slice in the simulation. The density field shows some traces of filamentary structure, and the temperature field is almost isothermal in high density regions.

In Figure 14, we show the fraction of mass contours of baryonic matter with various density and temperature. This figure summarizes the thermal state of the intergalactic medium. From this figure we know that most of the baryonic matter stays at the average density and in a temperature range of $10^4 - 10^6$ K. Only a small fraction of the baryonic matter is in high density regions, and that at high density regions remains at high temperatures ($> 10^7$ K). The material at underdense regions is cold ($T < 10^5$

K). The heating and cooling processes change the thermal state of intergalactic medium dramatically. One important feature is that the gas at high density region can actually stay very cold. The line indicating the heating and cooling balance in Figure 6 indicates the thermal states of these high density, low temperature gas. Our simulations with heating and cooling processes actually have some fraction of gas in these states.

5. Summary and Discussion

In this paper, we described a new cosmological N-body + gas dynamics code based on algorithms for an adaptive, unstructured mesh. The novel elements of this code are: (1) the mesh construction; (2) solving N-body systems; (3) solving hydrodynamic equations; (4) time step estimation and time integration; (5) mesh refinement; and (6) relevant heating and cooling processes for primordial gas.

The mesh construction with periodic boundary conditions is performed using a combined Bowyer-Watson algorithm and local transformation algorithm. The initial mesh for cosmological simulations is a uniform, staggered mesh. When some refining grids are required, new grid points are added to the mesh structure through the incremental Bowyer-Watson algorithm, which modifies the previous mesh structure slightly. The incorporation of mesh refinement in unstructured mesh gives one way to achieve high spatial resolution at relatively low cost. For best results, a good refinement criterion is essential. In general, refinement criterion can be derived both on physical and numerical bases.

Poisson's equation is discretized on an unstructured mesh and solved using conjugate gradient method. Particles are interpolated to the mesh nodes using linear interpolation. The resulting N-body algorithm is similar to the Particle-Mesh method with CIC interpolation. Because each node in an unstructured mesh has more associated cells, the new N-body algorithm has slightly higher force resolution than the PM algorithm.

We solve Euler's equations using finite-volume method. Flux functions are calculated using BGK gas-kinetic scheme. The gas-kinetic scheme constructs a time dependent distribution in the middle of an edge and calculate flux functions by moments of the distribution function. This scheme provides high resolution for shock capturing and is very stable for high Mach number flows.

The new cosmological code solves dark matter and gas dynamics with the same resolution. Our tests demonstrate that this code can provide high spatial resolution by mesh refinement. We include relevant cooling and heating processes for the primordial gas to simulate the evolution of intergalactic medium accurately.

Since the internal data structures for an unstructured mesh are homogeneous, unstructured mesh codes can be easily parallelized. The difficult part of parallelization is the Delaunay triangulation procedure. A parallel version of the code is being developed using the portable Message Passing Interface (MPI) library functions.

The author would like to thank Michael Norman for suggesting the investigation of unstructured mesh schemes, and Timothy J. Barth for kindly providing many references and some discussions. I greatly appreciate numerous detailed discussions with Kun Xu about the gas-kinetic scheme and sharing opinions about computational fluid dynamics. It is a great pleasure to thank Lars Hemquist and Jeremiah P. Ostriker for their support and encouragement. This work is supported by the NSF grant ASC 93-18185 awarded to the Grand Challenge Cosmology Consortium.

A . Geometric Relations for Unstructured Meshes

For unstructured meshes, we need to determine the relation between a point and a simplex (triangle or tetrahedron), and also some geometric quantities, like the volume of a simplex and the surface area of its faces. In this appendix, we give the formulas to calculate these quantities generally in n -dimensional space.

Let $p_1; p_2; \dots, p_{n+1}$ be $n+1$ distinct points in n -dimensional space. The n -dimensional volume of the simplex T with vertices $p_1; \dots, p_{n+1}$ is given by

$$\text{Vol}(p_1; \dots, p_{n+1}) = \frac{1}{n!} \det \begin{pmatrix} 1 & 1 & \dots & 1 \\ p_1 & p_2 & \dots & p_{n+1} \end{pmatrix} \quad (\text{A } 1)$$

Let q be an arbitrary point in n -space. If the simplex T with vertices $p_1; \dots, p_{n+1}$ is nondegenerate, i.e., if $\text{Vol}(p_1; \dots, p_{n+1}) \neq 0$, the numbers, $b_1; b_2; \dots, b_{n+1}$, satisfying

$$\begin{pmatrix} 1 & 1 & \dots & 1 \\ p_1 & p_2 & \dots & p_{n+1} \end{pmatrix} \begin{pmatrix} b_1 \\ b_2 \\ \vdots \\ b_{n+1} \end{pmatrix} = \begin{pmatrix} 1 \\ q \end{pmatrix} \quad (\text{A } 2)$$

are called barycentric coordinates of a point q relative to simplex T . It can be shown that,

$$b_k = \frac{\det(p_1; \dots, q; \dots, p_{n+1})}{\det(p_1; \dots, p_k; \dots, p_{n+1})} \quad (\text{A } 3)$$

Obviously, b_k is a linear function of q . Thus, b_k indicates the position of q relative to the hyperplane H_k containing the facet of simplex T opposite to vertex p_k . $b_k = 0$ when q is in

$H_k, b_k > 0$ when q is on the same side of H_k from p_k , and $b_k < 0$ when q is on the opposite side of H_k from p_k . As a consequence, we know that the point q is inside simplex T if and only if all $b_k \geq 0$. The surface area vector S_k of hyperplane H_k with its direction pointing away from p_k is

$$S_k = \text{Vol}(T) r b_k(x); \quad (\text{A } 4)$$

It can be shown that the integration of function $f(x_1; \dots, x_n)$ over the volume of a simplex T can be expressed as,

$$\int_T f(x; y; z) d^n x = \text{Vol}(T) n! \int_0^1 \int_0^{1-b_1} \int_0^{1-b_1-b_{n-1}} \dots \int_0^{1-b_1-b_{n-1}} f(x_1; \dots, x_n) x \quad (\text{A } 5)$$

If a simplex T is non-degenerate, it has a unique circumsphere S . Given an arbitrary point q in n -space, we can determine if q is inside, outside or on the sphere S by the following function,

$$\text{InSphere}(q; T) = \frac{\det \begin{pmatrix} 0 & 1 & 1 & \dots & 1 \\ 1 & w_q & w_1 & \dots & w_{n+1} \\ q & p_1 & \dots & p_{n+1} \end{pmatrix}}{\det \begin{pmatrix} 1 & 1 & \dots & 1 \\ p_1 & p_2 & \dots & p_{n+1} \end{pmatrix}}; \quad (\text{A } 6)$$

where $w_p = \sum_{i=0}^n x_{p,i}^2$. $\text{InSphere}(q; T) > 0$ when q is inside S , $\text{InSphere}(q; T) = 0$ when q is on S and $\text{InSphere}(q; T) < 0$ when q is outside S . When calculating the value of $\text{InSphere}(q; T)$, we should be aware of round-off errors (Barth 1995), because the result of triangulation could be wrong due to floating point inaccuracies. To avoid the problems caused by floating point round-off errors, we calculate the above $\text{InSphere}(T; q)$ function using the following formula instead,

$$\text{InSphere}(T; q) = \frac{\det \begin{pmatrix} w_1^0 & w_2^0 & \dots & w_{n+1}^0 \\ p_1^0 & p_2^0 & \dots & p_{n+1}^0 \end{pmatrix}}{\det \begin{pmatrix} 1 & 1 & \dots & 1 \\ p_1^0 & p_2^0 & \dots & p_{n+1}^0 \end{pmatrix}} \cdot \frac{1}{\min_{k=1,2,\dots,n+1} (w_k^0)}; \quad (\text{A } 7)$$

where $p_k^0 = p_k - q$ and $w_k^0 = \sum_{i=0}^n x_{p,i}^2$. The value of the above function is compared with a small number ϵ , instead of 0, to determine the result of the sphere test. For single precision floating operations, we use $\epsilon = 10^{-4}$. Our numerical experiments show that the above estimate is sufficient to give the correct Delaunay triangulation. Another way to avoid the round-off error is use exact redundant expression calculation (see Barth 1995 for more discussions). But there are a lot of extra calculations related to the exact redundant expression Fortune & van Wyk 1993.

B . Coe ficient calculation in BGK formalism

In this appendix, we will give detailed formulas to calculate the coefficients $A^L, A^R, A^{GL}, A^{GR}, B$, and other quantities for the BGK scheme described earlier in the paper.

At the beginning of each time step, we know the fluid state at the two ends of each edge U^L and U^R . The interpolated fluid state in the middle of the edge, U^L and U^R , which are interpolated from left side and right side respectively, can be constructed from the SLIP (Symmetric Limited Positive) formulation (Jamson 1995), which is derived from the local extremum diminishing (LED) principle. The constructed fluid state can be expressed as,

$$U^L = U^L + \frac{1}{2}e^L; \text{ and } U^R = U^R + \frac{1}{2}e^R; \quad (B1)$$

where $e_{;j} = L(U_{;j+1=2}; U_{;j-1=2})$ is the limited average, $L(u;v)$ is a limiter, and $U_{;j+1=2} = U_{;j+1} - U_{;j}$. An example is the van Leer limiter, $L(u;v) = \frac{2uv}{u+v}$ when $u-v > 0$, and $L(u;v) = 0$ otherwise. The equilibrium distribution functions g_0^L and g_0^R are constructed from U^L and U^R respectively.

The macroscopic quantities are moments of distributions. We have $U^L(x) = \int_{-\infty}^{\infty} g^L(1 + A^L x) dx$. For compatibility, we require $U^L(x = \frac{1}{2}) = U^L$. After some algebra, we get the solutions of the coefficients A^L and A^R ,

$$\langle \cdot \rangle^L A^L = e^L \text{ and } \langle \cdot \rangle^R A^R = e^R; \quad (B2)$$

The notation $\langle \cdot \rangle$ will be defined later in Appendix C.

The constructed fluid state at the middle of an edge U^G is defined to be,

$$U^G = \int_{-\infty}^{\infty} f_0 dx = \int_{u_x > 0} g_0^L dx + \int_{u_x < 0} g_0^R dx; \quad (B3)$$

The equilibrium distribution g_0^G is constructed from U^G . Taking the limit $t \rightarrow 0$, we have $U^G(x) = \int_{-\infty}^{\infty} g^G(1 + A^G x) dx$. For $x = \frac{1}{2}$, we require $U^G(\frac{1}{2}) = U^L$ and $U^G(\frac{1}{2}) = U^R$. This gives the solutions of coefficients A^{GL} and A^{GR} .

The distribution functions $f(t; x; u)$ and $g(t; x; u)$ must be compatible with each other. Conservation laws give the following compatibility condition,

$$\int_{-\infty}^{\infty} (f - g) du = 0; \quad (B4)$$

Applying the integrated solution of $f(t; x; u)$ (equation 14) to the above compatibility equation and integrate over the whole time step T , we have,

$$0 = \int_{-\infty}^{\infty} du \frac{1}{dt} \int_0^T (f - g) dt$$

$$\begin{aligned}
= & \frac{h}{1} e^{T=0} \frac{i}{U^G} \\
& + \frac{h}{2} (1 - e^{T=0}) \frac{i}{T} (1 + e^{T=0}) \langle u_x \rangle_{u>0}^G A^{GL} + \langle u_x \rangle_{u<0}^G A^{GR} \\
& + \frac{h}{T} + \frac{i}{(1 - e^{T=0})} \langle \dots \rangle^G B \\
& + \frac{h}{1} e^{T=0} \langle \dots \rangle_{u>0}^L + \langle \dots \rangle_{u<0}^R \\
& \frac{h}{(T + \dots)} e^{T=0} \frac{i}{A^L} \langle u \rangle_{u>0}^L + A^R \langle u \rangle_{u<0}^R
\end{aligned} \tag{B5}$$

These equations give the solutions to the coefficients B_{α} .

For convenience, we give the formula to calculate the time integrated ux functions,

$$\begin{aligned}
& \int_0^T F(0;t) dt \int_0^T dt \int_i u f(t;0;u) du \\
&= \frac{1}{T} \frac{1}{h} (1 - e^{-T/h}) \langle u \rangle^G \\
&+ \frac{1}{h} \frac{1}{2} (1 - e^{-T/h}) \frac{1}{T} (1 + e^{-T/h}) A^{GL} \langle u^2 \rangle_{u>0}^G + A^{GR} \langle u^2 \rangle_{u<0}^G \\
&+ \frac{1}{T^2} \frac{1}{h} \frac{1}{2} (1 - e^{-T/h}) B \langle u \rangle_i^G \\
&+ \frac{1}{T} e^{-T/h} \langle u \rangle_{u>0}^L + \langle u \rangle_{u<0}^R \\
&+ \frac{1}{(T + h)} e^{-T/h} A^L \langle u^2 \rangle_{u>0}^L + A^R \langle u^2 \rangle_{u<0}^R
\end{aligned} \tag{B.6}$$

The collision time can be derived from classical statistical mechanics to be the mean free path divided by the rms velocity of atoms. We use the following formula to estimate

$$= C_1 \frac{p_-}{p^L + p^R} + C_2 T \frac{\dot{p}^L p^R}{p^L + p^R}; \quad (\text{B } 7)$$

where Δt is the time step and C_1, C_2 are constants. We take $C_1 = 0.01$ and $C_2 = 1$ in our calculations. The results are not sensitive to the choice of the actual values of C_1, C_2 .

C. Velocity moments

We define the moment of a quantity w of the equilibrium state g_0 as the following,

$$\langle w \rangle = \frac{1}{Z} w_{g_0} \text{dud} = \frac{1}{Z} w_{De}^{(u,v)^{-2+2}} \text{dud} \quad (C1)$$

where V is the macroscopic velocity, $p = 2p$ is the gas temperature, and $D = \left(\frac{m}{2\pi} \right)^{(K+N)/2}$ is the normalization factor. Here, K is the degree of the internal variable and N is the space dimension Xu 1993. For a polytropic gas, classical statistical mechanics gives $\gamma = (n+2)/n$, where n is the total number of effective degrees of freedom

of the molecule: thus a monoatomic gas has $n = 3$, $f = 5=3$, and a diatomic gas with two rotational degrees of freedom has $n = 5$, $f = 7=5$. For a flow in N -dimensional space, we have $K = n - N = \frac{2}{1} - N$.

Following the above definition, we obtain the iterative relation,

$$\langle u^{n+2} \rangle = V \langle u^{n+1} \rangle + \frac{n+1}{2} \langle u^n \rangle; \quad (C2)$$

and the following specific values of moments,

$$\langle u^0 \rangle = 1 \quad (C3)$$

$$\langle u^1 \rangle = V \quad (C4)$$

$$\langle u^2 \rangle = \frac{K}{2} \quad (C5)$$

$$\langle u^4 \rangle = \frac{K(K+2)}{4^2} \quad (C6)$$

$$\langle u^6 \rangle = \frac{K(K+2)(K+4)}{8^3} \quad (C7)$$

For velocity moments involving integration over half of the velocity space, the above iterative relation (equation C2) still holds true, except for the following first few moments,

$$\langle u_x^0 \rangle_{u_x > 0} = \frac{1}{2} \text{erfc}\left(\frac{p - V_x}{\sqrt{2}}\right) \quad (C8)$$

$$\langle u_x^1 \rangle_{u_x > 0} = V_x \frac{1}{2} \text{erfc}\left(\frac{p - V_x}{\sqrt{2}}\right) + \frac{e^{-\frac{V_x^2}{2}}}{\sqrt{2}} \quad (C9)$$

$$\langle u_x^0 \rangle_{u_x < 0} = \frac{1}{2} \text{erfc}\left(\frac{p - V_x}{\sqrt{2}}\right) \quad (C10)$$

$$\langle u_x^1 \rangle_{u_x < 0} = V_x \frac{1}{2} \text{erfc}\left(\frac{p - V_x}{\sqrt{2}}\right) - \frac{e^{-\frac{V_x^2}{2}}}{\sqrt{2}} \quad (C11)$$

The moments of u^n and u^n can be derived from the moments of u^n and u^n . We explicitly write them out for reference.

$$\langle u^n \rangle = \frac{1}{\sqrt{2\pi}} \int_{-\infty}^{\infty} u^n \text{De}^{-\frac{(u-V)^2}{2}} du \quad (C12)$$

$$\begin{aligned} &= \frac{1}{\sqrt{2\pi}} \left(\int_{-\infty}^0 u^n \text{De}^{-\frac{(u-V)^2}{2}} du + \int_0^{\infty} u^n \text{De}^{-\frac{(u-V)^2}{2}} du \right) \\ &= \frac{1}{\sqrt{2\pi}} \left(\int_{-\infty}^0 u^n \text{De}^{-\frac{(u-V)^2}{2}} du + \int_0^{\infty} u^n \text{De}^{-\frac{(u-V)^2}{2}} du \right) \\ &= \frac{1}{\sqrt{2\pi}} \left(\int_{-\infty}^0 u^n \text{De}^{-\frac{(u-V)^2}{2}} du + \int_0^{\infty} u^n \text{De}^{-\frac{(u-V)^2}{2}} du \right) \\ &= \frac{1}{\sqrt{2\pi}} \left(\int_{-\infty}^0 u^n \text{De}^{-\frac{(u-V)^2}{2}} du + \int_0^{\infty} u^n \text{De}^{-\frac{(u-V)^2}{2}} du \right) \end{aligned} \quad (C13)$$

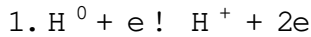
{ 19 {

$$= \begin{matrix} 0 & & & & 1 \\ & < u^n > & < u^{n+1} > & & \frac{1}{2} < u^{n+2} + u^{n-2} > \\ & < u^{n+1} > & < u^{n+2} > & & \frac{1}{2} < u^{n+3} + u^{n+1-2} > \\ \frac{1}{2} < u^{n+2} + u^{n-2} > & \frac{1}{2} < u^{n+3} + u^{n+1-2} > & \frac{1}{4} < u^{n+4} + 2u^{n+2-2} + u^{n-4} > \end{matrix}$$

For moments of u^n and u^n integrating over half velocity space, the above expressions are still good except that one must be aware that $\langle u^0 \rangle$ may not equal to 1 in the above formulas.

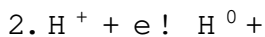
D . Cooling Rates and Reaction Coefficients

Various cooling processes relevant to primordial baryonic matter have been included in the code. Primordial gas is assumed consist essentially entirely of hydrogen and helium. The relevant cooling and heating processes are: bremsstrahlung emission, collisional excitation of H_0 and $H e^+$, collisional ionization of H_0 , $H e^0$ and $H e^+$, radiative recombination of H^+ , $H e^+$ and $H e^{++}$, and dielectronic recombination of $H e^+$. Ionization equilibrium is assumed to determine the fraction in each species. The reaction rates k_i (in unit of sec^{-1}) and the related cooling rates λ_i (in unit of $\text{erg cm}^3 \text{sec}^{-1}$) are listed below (c.f. Black 1981, Cen 1992, Katz, Weinberg, & Hemquist 1996 and Abelet al. 1996), (Note that $T_n = T = 10^4 \text{K}$.)



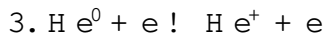
$$k_1 = 5.85 \cdot 10^{11} T^{1=2} e^{157809.1/T} (1 + T_5^{1=2})^{-1}$$

$$\lambda_1 = 1.27 \cdot 10^{21} T^{1=2} e^{157809.1/T} (1 + T_5^{1=2})^{-1} n_e n_{H^0}$$



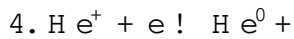
$$k_2 = 8.40 \cdot 10^{11} T^{1=2} T_3^{0.2} (1 + T_6^{0.7})^{-1}$$

$$\lambda_2 = 8.70 \cdot 10^{27} T^{1=2} T_3^{0.2} (1 + T_6^{0.7})^{-1} n_e n_{H^+}$$



$$k_3 = 2.38 \cdot 10^{11} T^{1=2} e^{285335.4/T} (1 + T_5^{1=2})^{-1}$$

$$\lambda_3 = 9.38 \cdot 10^{22} T^{1=2} e^{285335.4/T} (1 + T_5^{1=2})^{-1} n_e n_{H e^0}$$



$$k_4 = 1.5 \cdot 10^{10} T^{6.353}$$

$$\lambda_4 = 1.55 \cdot 10^{26} T^{0.3647} n_e n_{H e^+}$$

{ 20 {

5. $H e^+ + e \rightarrow H e^{++} + 2e$

$$k_5 = 5.68 \cdot 10^{12} T^{1=2} e^{631515.0=T} (1 + T_5^{1=2})^{-1}$$

$$_5 = 4.95 \cdot 10^{22} T^{1=2} e^{631515.0=T} (1 + T_5^{1=2})^{-1} n_e n_{H e^+}$$

6. $H e^{++} + e \rightarrow H e^+ +$

$$k_6 = 3.36 \cdot 10^{10} T^{1=2} T_3^{0.2} (1 + T_6^{0.7})^{-1}$$

$$_6 = 3.48 \cdot 10^{26} T^{1=2} T_3^{0.2} (1 + T_6^{0.7})^{-1} n_e n_{H e^{++}}$$

7. $H e^+ + 2e \rightarrow H e^0 + e$

$$k_7 = 1.9 \cdot 10^3 T^{1.5} e^{470000.0=T} (1 + 0.3e^{94000.0=T})$$

$$_7 = 1.24 \cdot 10^{13} T^{1.5} e^{470000.0=T} (1 + 0.3e^{94000.0=T}) n_e n_{H e^+}$$

8. collisional excitation of H^0

$$_8 = 7.50 \cdot 10^{19} e^{118348.0=T} (1 + T_5^{1=2}) n_e n_{H^0}$$

9. collisional excitation of $H e^+$

$$_9 = 5.54 \cdot 10^{17} T^{3.97} e^{473638.0=T} (1 + T_5^{1=2})^{-1} n_e n_{H e^+}$$

10. bremsstrahlung

$$_{ff} = 1.42 \cdot 10^{27} g_{ff} T^{1=2} n_e (n_{H^+} + n_{H e^+} + 4n_{H e^{++}})$$

$$g_{ff} = 1.1 + 0.34 \exp[(5.5 - \log T)^2 = 3.0]$$

When an ultraviolet (UV) background radiation field is present, photoionization of H^0 , $H e^0$ and $H e^+$ is also included. The photoionization rates are defined by

$$_i = \int_{\nu_i}^{\infty} \frac{4 J(\nu)}{h} \sigma_i(\nu) d\nu; \quad (D 1)$$

where $J(\nu)$ is the intensity of the UV background, ν_i is the threshold frequency and $\sigma_i(\nu)$ is the photoionization cross section for species i . The heating rate associated with photoionization is

$$H = n_{H^0} \epsilon_{H^0} + n_{H e^0} \epsilon_{H e^0} + n_{H e^+} \epsilon_{H e^+} \text{ erg cm}^{-3} \text{ sec}^{-1}; \quad (D 2)$$

where

$$\int_0^z \frac{4 J(\nu)}{h} \nu^3 (h\nu - h_i) d\nu : \quad (D 3)$$

Besides these radiative cooling processes, we include inverse Compton cooling of the microwave background. The inverse Compton cooling rate is given by (Ikeuchi & Ostriker 1986),

$$c = 5.41 \cdot 10^{36} n_e T (1+z)^4 \text{ erg cm}^{-3} \text{ sec}^{-1} : \quad (D 4)$$

REFERENCES

- Abel, T., Anninos, P., Zhang, Y., & Norman, M. L. 1996, astro-ph/9608040
- Barnes, J., & Hut, P. 1986, Nature, 324, 446
- Barth, T. J. 1995, Aspects of Unstructured Grids and Finite-Volume Solvers for the Euler and Navier-Stokes Equations, VKI Lecture series (unknown)
- Berger, M., & Colella, P. 1989, J. of Computational Physics, 82, 64
- Bhatnagar, P., Gross, E., & Krook, M. 1954, Physical Review, 94, 511
- Black, J. 1981, MNRAS, 197, 553
- Bowyer, A. 1981, The Computer Journal, 24, 162
- Cen, R. 1992, ApJS, 78, 341
- Cen, R., & Ostriker, J. 1993, ApJ, 417, 404
- Efstathiou, G., Davis, M., Frenk, C. S., & White, S. D. M. 1985, ApJS, 57, 241
- Fortune, S., & van Wyk, C. J. 1993, in Proceedings of the 9th Annual Symposium on Computational Geometry, 163
- Frenk, C., et al. 1996, in preparation
- Green, P. J., & Sibson, R. 1977, The Computer Journal, 21, 168
- Hemquist, L. 1987, ApJS, 64, 715
- Hemquist, L., & Katz, N. 1989, ApJS, 70, 419

- Hockney, R.W ., & Eastwood, J.W . 1981, Computer Simulation Using Particles (New York: McGraw Hill)
- Ikeuchi, S., & Ostriker, J.P. 1986, ApJ, 301, 522
- Jam eson, A . 1995, Int. J. for Numerical Methods in Fluids, 20, 743
- Joe, B . 1989, SIAM Journal Scientific and Statistical Computation, 10, 718
- K allinderis, Y ., & Vijayan, P . 1993, AIAA Journal, 31, 1440
- K atz, N ., Weinberg, D . H ., & Hernquist, L . 1996, ApJS, 105, 19
- K lein, R ., Colella, P ., & McKee, C . 1992, Advances in Compressible Turbulent Mixing, ed. W . Dannevik, A . Buckingham , & C . Leith (Washington DC : GPO), 452
- Law son, C . L . 1986, Computer Aided Geometric Design, 3, 231
- M avriplis, D . 1992, Unstructured Mesh Algorithms for Aerodynamic Calculations (unknown), 57
- Peebles, P . J. E . 1980, The Large Scale Structure of the Universe (Princeton University Press)
- Press, W . H ., Teukolsky, S. A ., Vetterling, W . T ., & Flannery, B . P . 1992, Numerical Recipes in C (Cambridge University Press)
- Ryu, D ., Ostriker, J. P ., Kang, H ., & Cen, R . 1993, ApJ, 414, 1
- Shu, F . 1991, The Physics of Astrophysics: Volume II. Gas Dynamics (University Science Books)
- Vijayan, P ., & K allinderis, Y . 1994, Journal of Computational Physics, 113, 249
- W atson, D . 1981, The Computer Journal, 24, 167
- X u, G . 1995, ApJS, 98, 355 (Paper I)
- X u, K . 1993, Ph D . thesis, Columbia University
- X u, K ., Martinelli, L ., & Jam eson, A . 1995, Journal of Computational Physics, 120, 48
- X u, K ., & Prendergast, K . 1994, J. Computational Physics, 114, 9

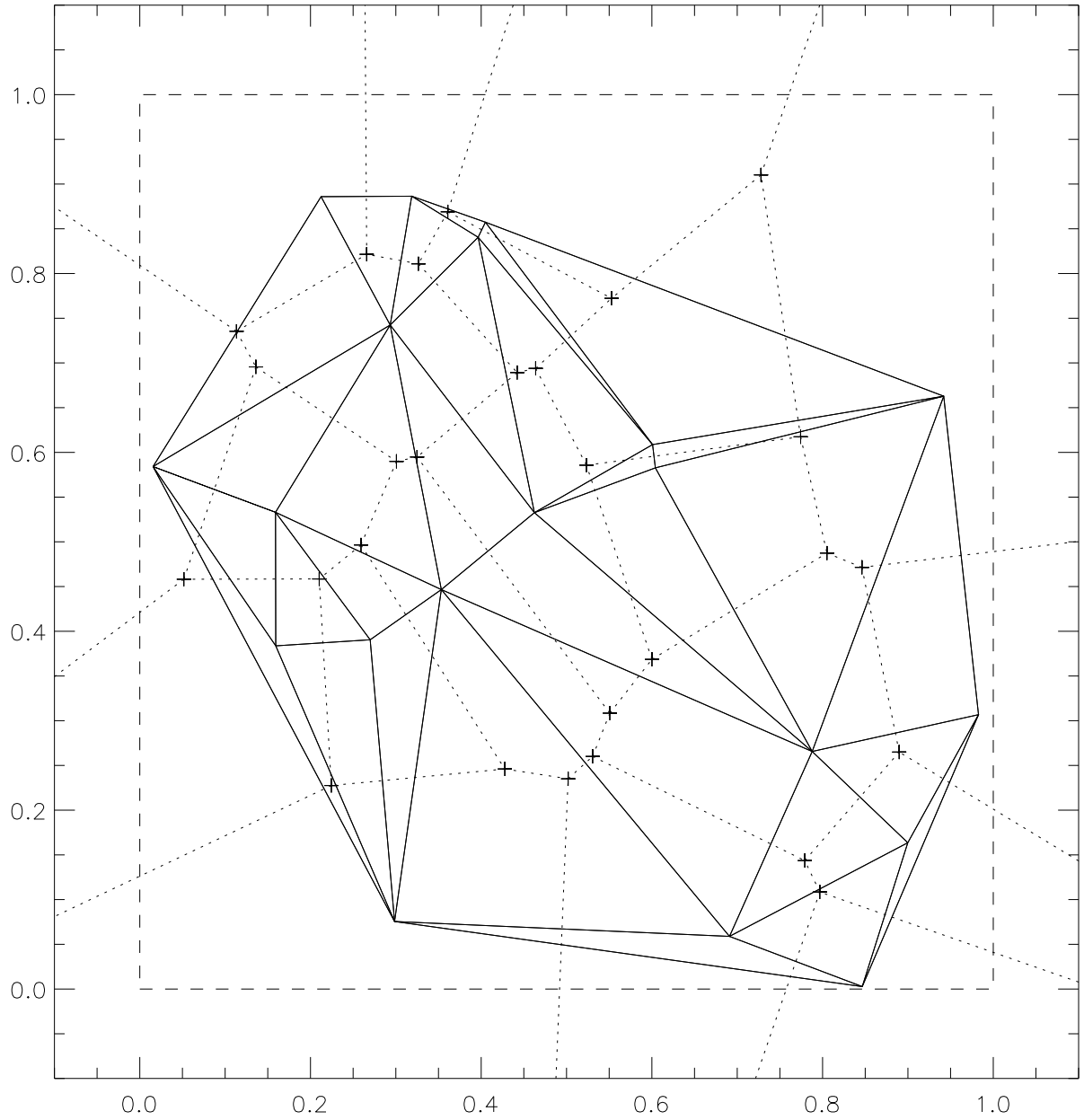


Fig. 1. | Relation between Dirichlet tessellation (dashed lines) and Delaunay triangulation (solid lines) in 2-dimensional space. The crosses indicate the center of circum centers of the corresponding triangles.

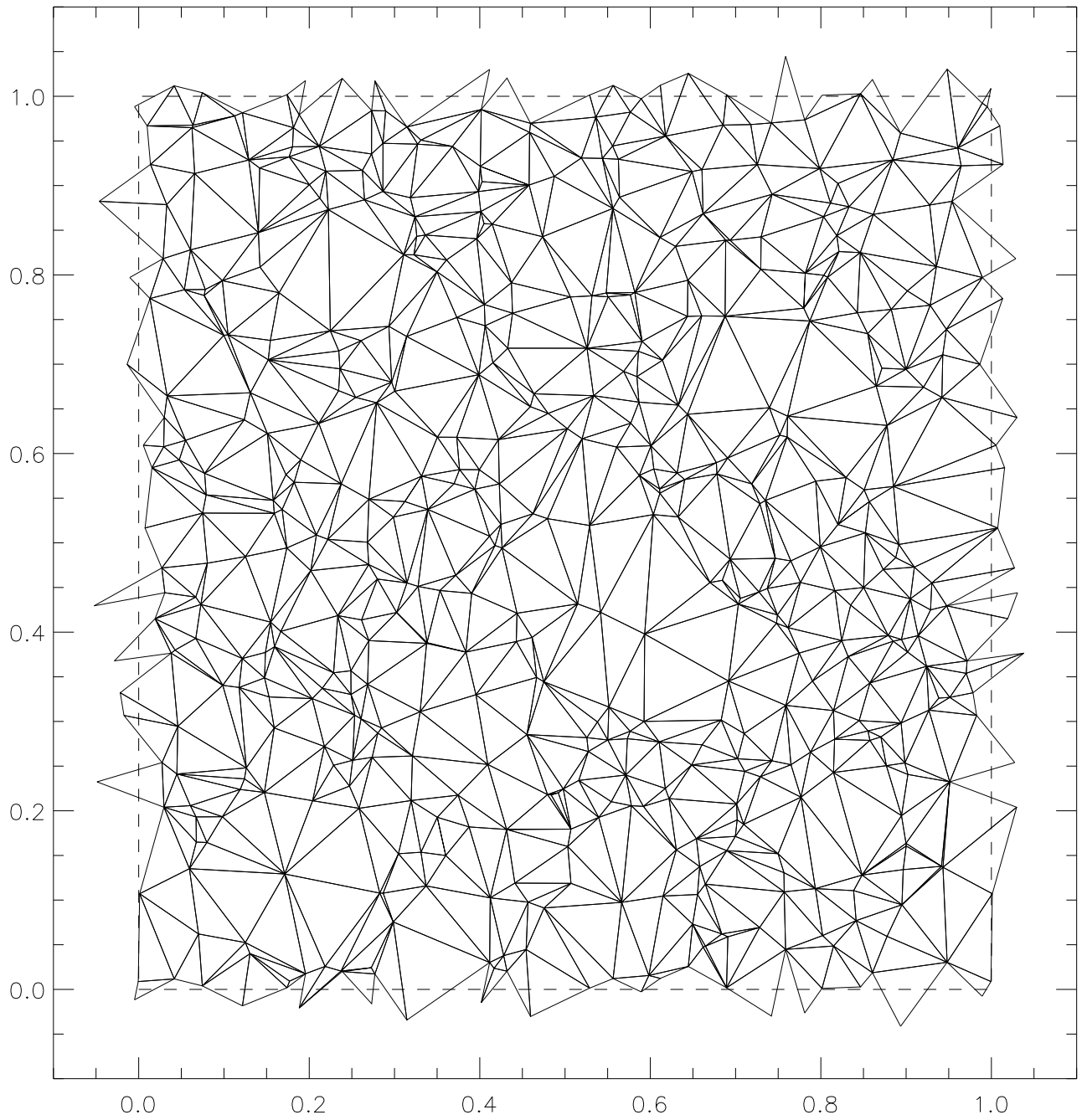


Fig. 2. | Example of 2-dimensional unstructured mesh constructed by Delaunay triangulation. 1000 nodes are randomly scattered in a periodic box whose borders are indicated by dashed lines.

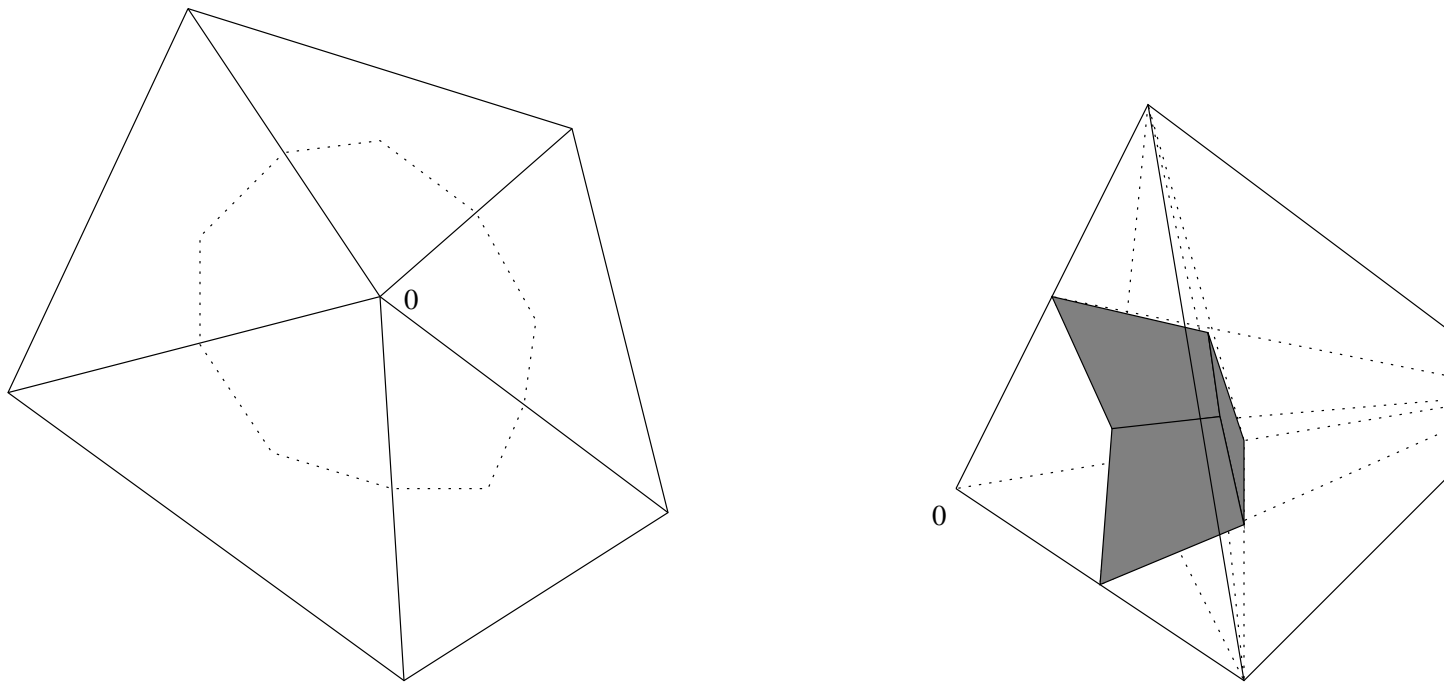


Fig. 3. | Illustration of control volume of node 0 with 2-D case on the left and 3-D case on the right. On the left panel, the dashed lines, which connects the centers of edges and the middle of triangles, indicates the control volume for node 0. On the right panel, only one tetrahedron associated with node 0 is shown. The shaded region represents one piece of the control volume boundaries.

{ 26 {

$N=32^3$

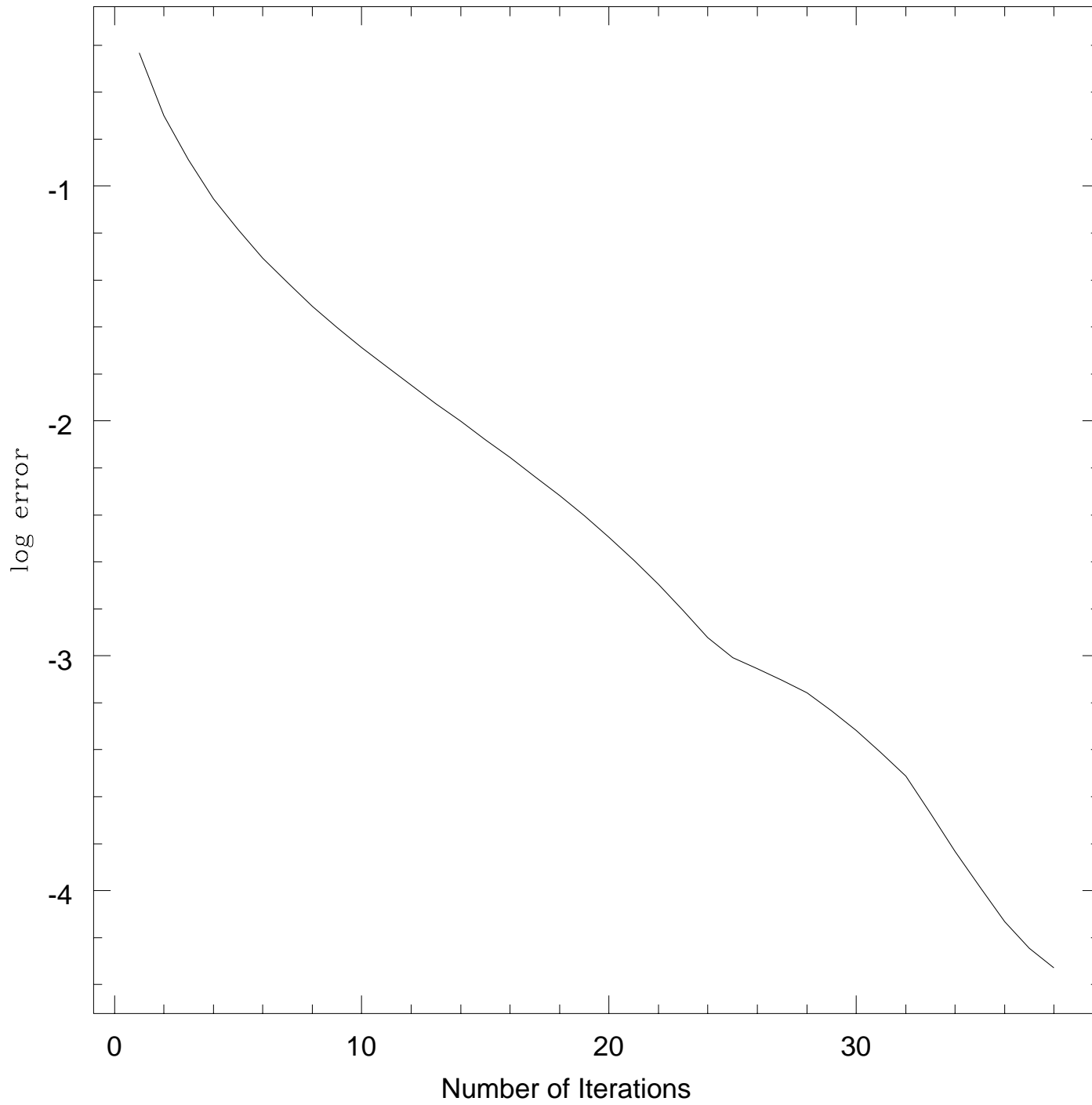


Fig. 4. The convergence rate of our conjugate gradient algorithm . The error decreases almost exponentially as the number of iterations.

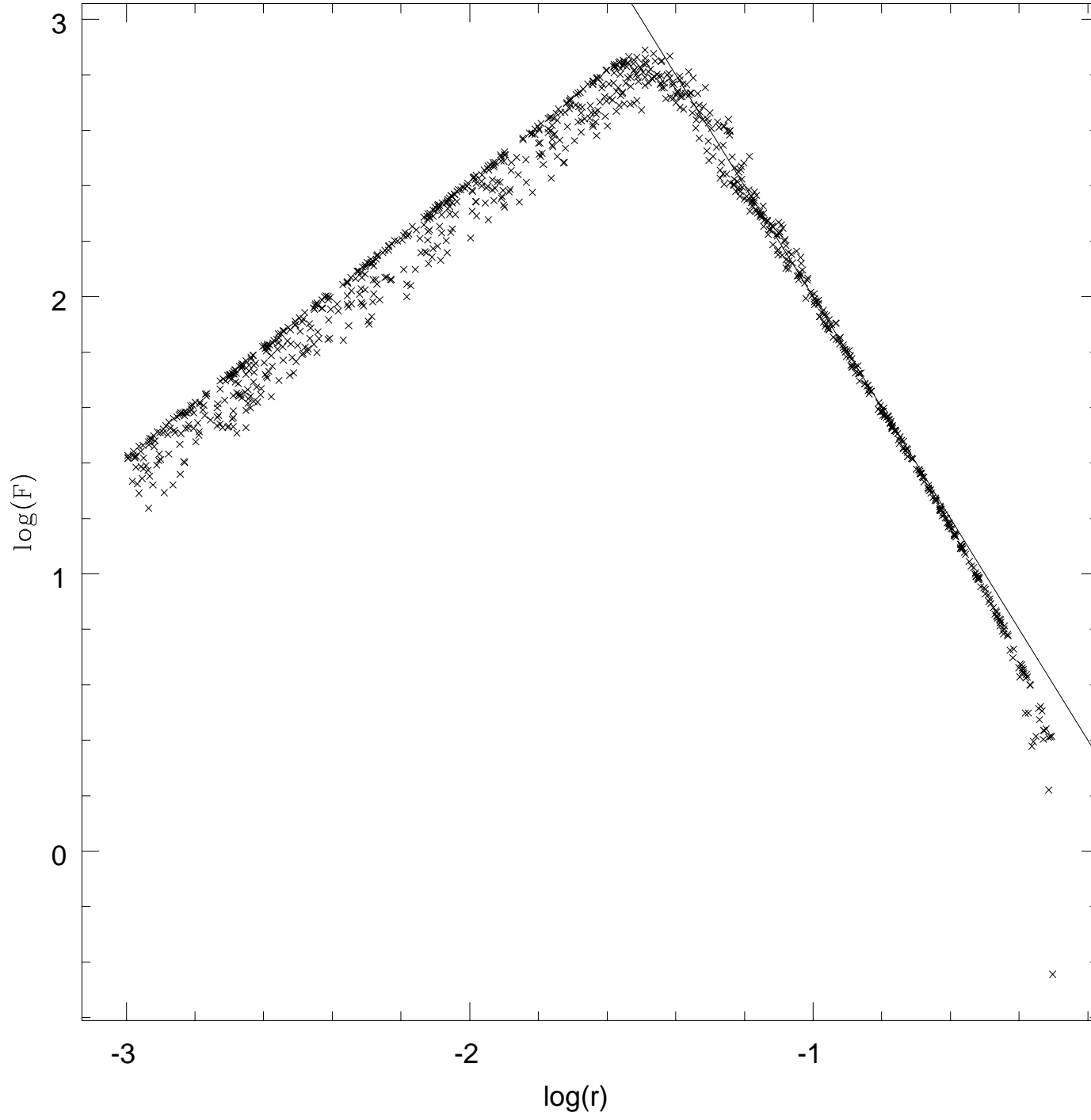


Fig. 5. The force between two particles on an unstructured mesh using 32^3 nodes. The 32^3 nodes distributed uniformly in a periodic box. The solid line indicates the r^{-2} law.

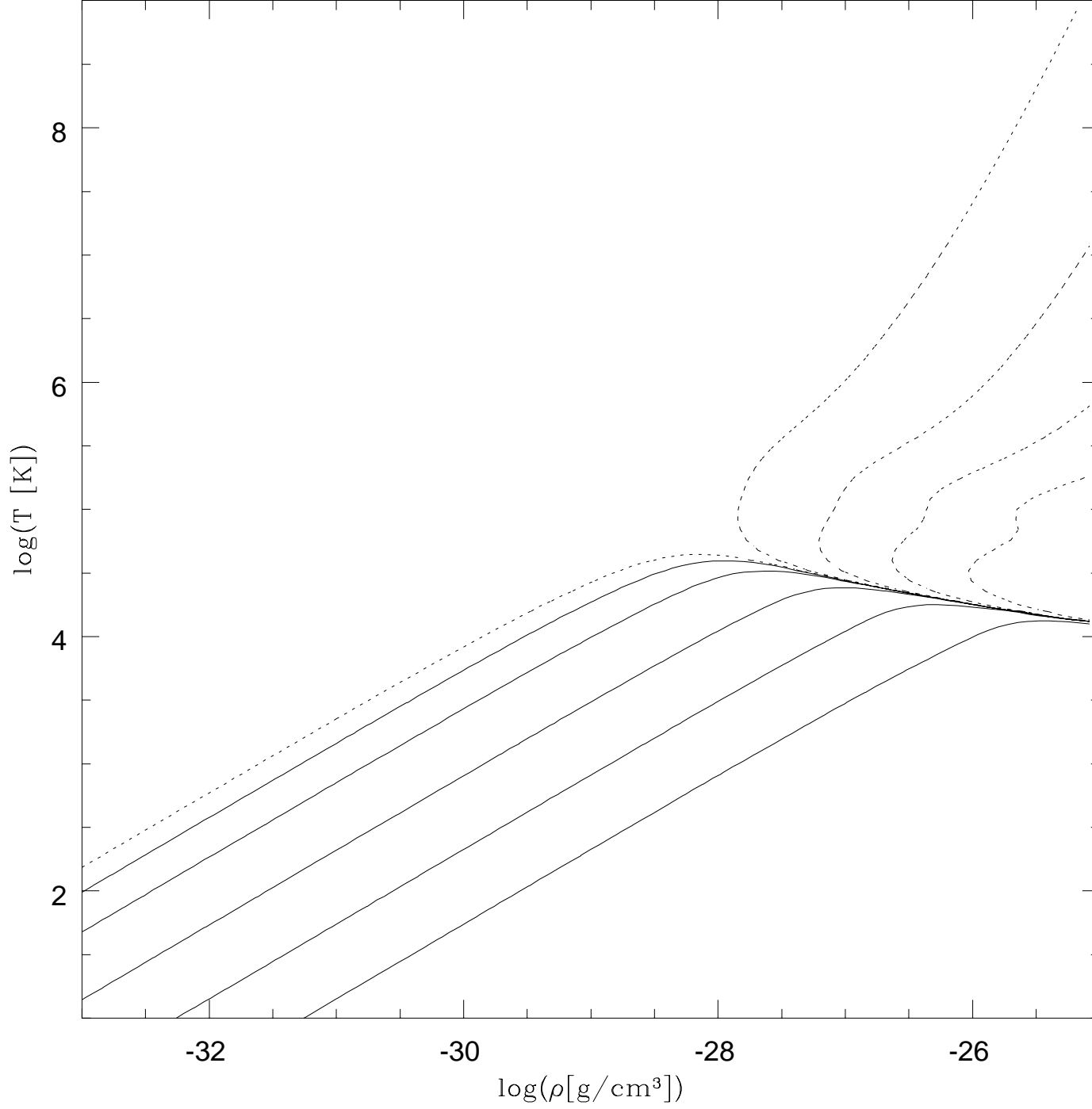


Fig. 6. Cooling time scale $t_{\text{cool}} = E = j \cdot j$ with radiative cooling, photoionization and inverse Compton cooling for gas at different density and temperature. The UV radiation is assumed to be $J(\nu) = 10^{22} (L_{\text{UV}} = 10^{44} \text{ erg/s}) \text{ erg/cm}^3/\text{sec/Hz}$, and the Compton cooling is calculated at $z = 2$.

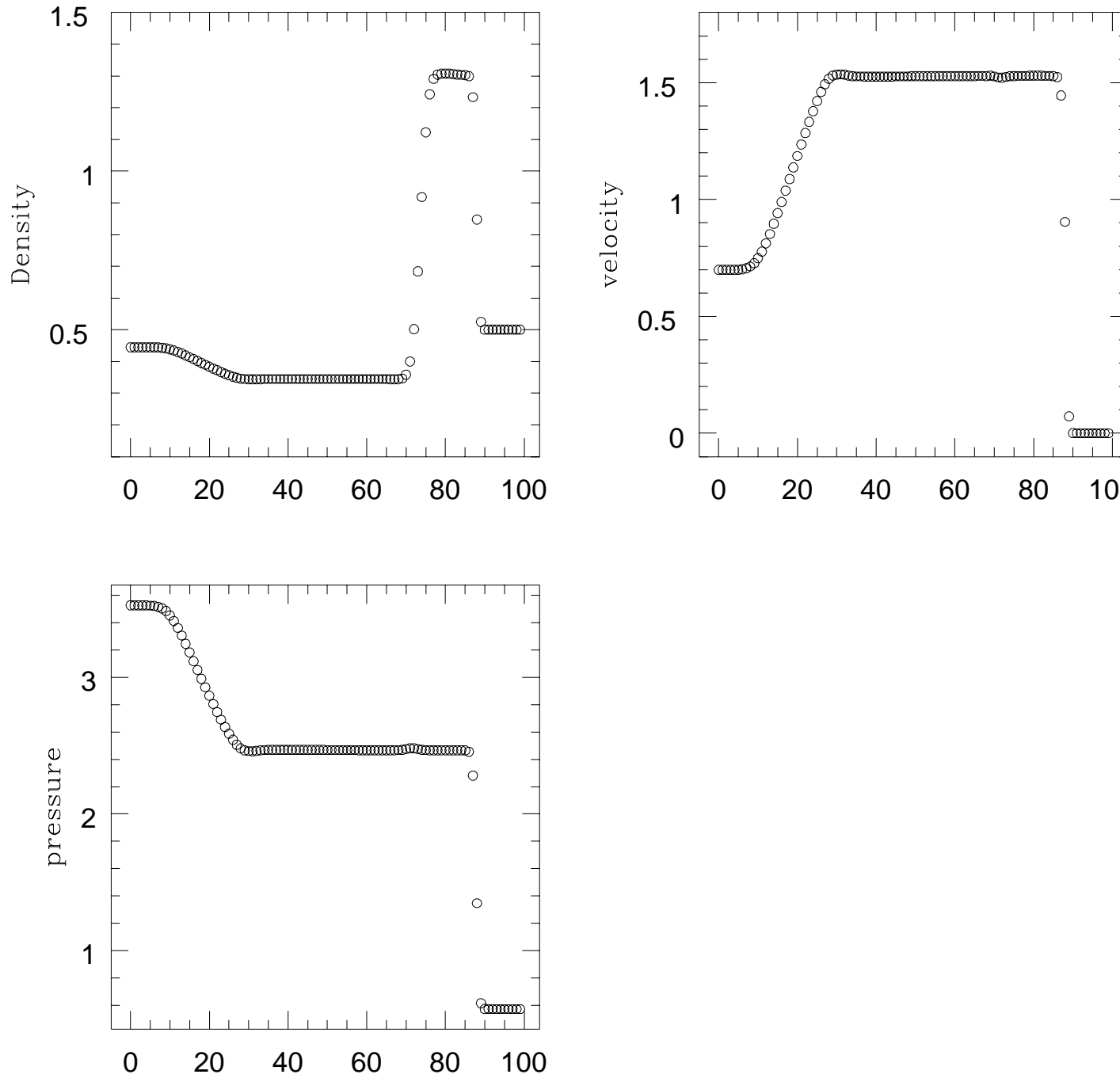


Fig. 7. | Lax shock tube test using the 1-dimensional BGK scheme. The result is at time $t = 0.15$. The BGK scheme captures shocks in two cells.

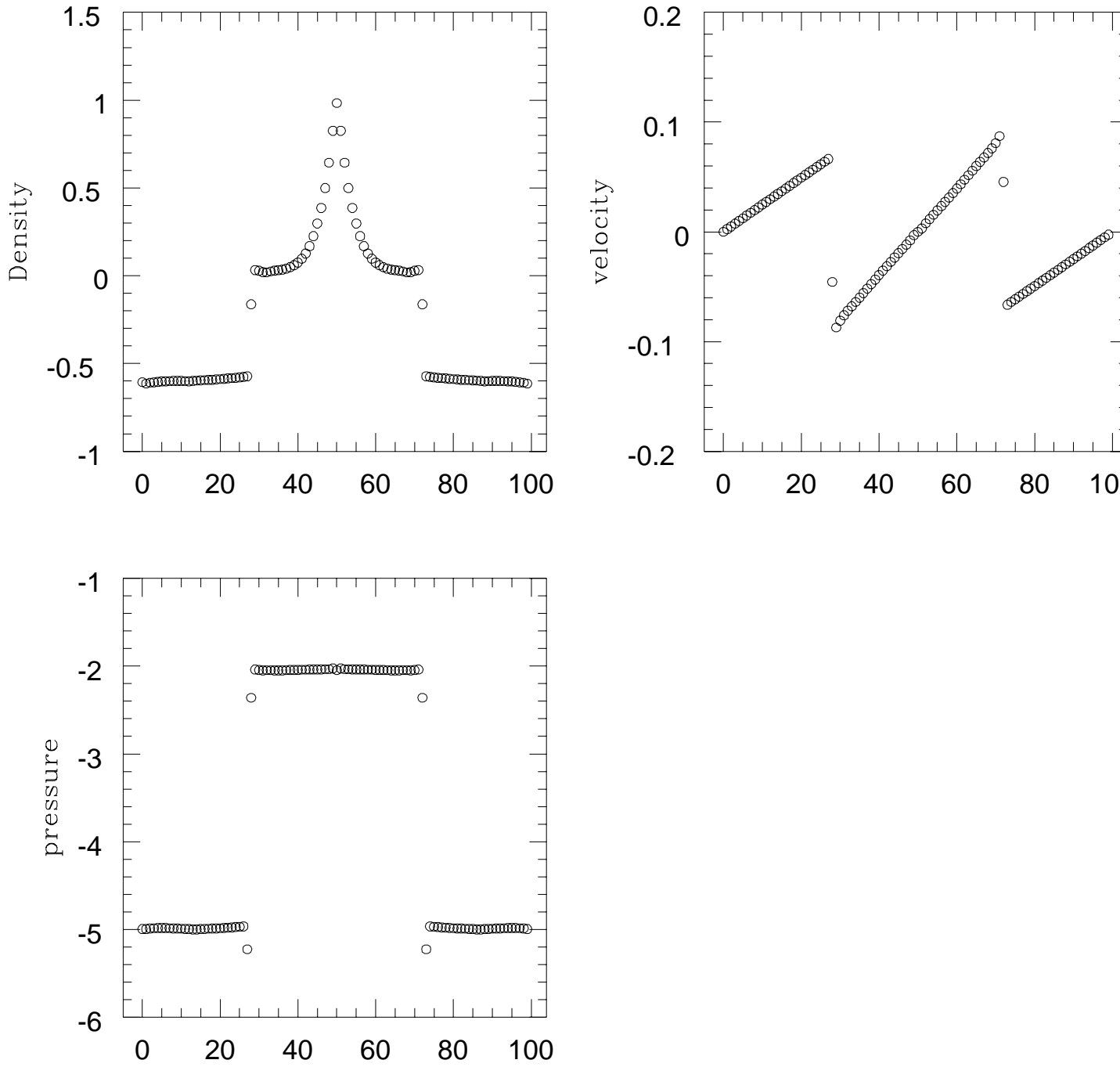


Fig. 8. One dimensional caustic test with BGK gas-kinetic scheme using 100 zones. The results are at $t = 3$.

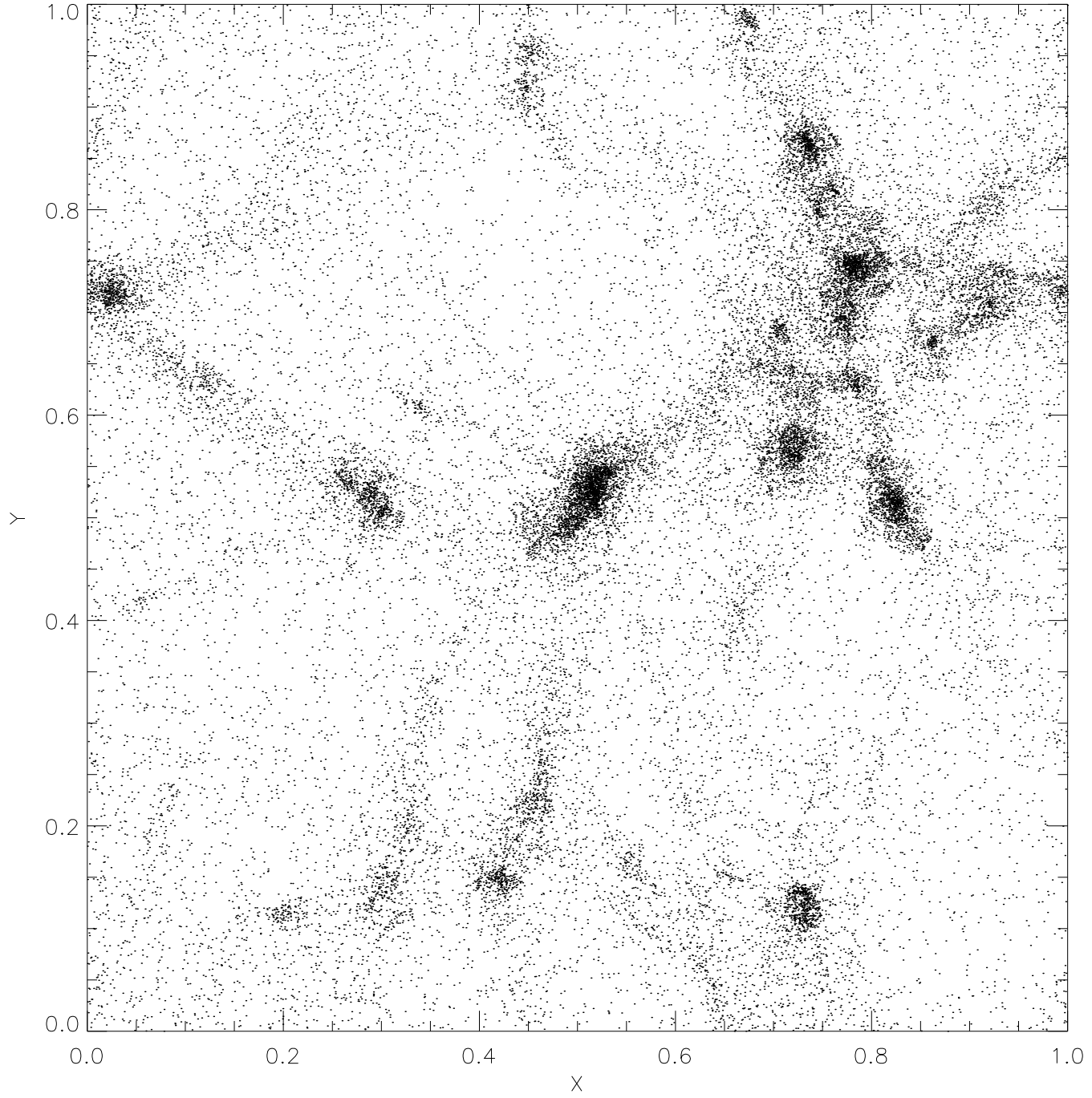


Fig. 9. Result of a pure N-body unstructured mesh simulation without mesh refinement. All the 32^3 particles are projected in the X-Y plane. The raw mesh is a 32^3 uniform mesh.

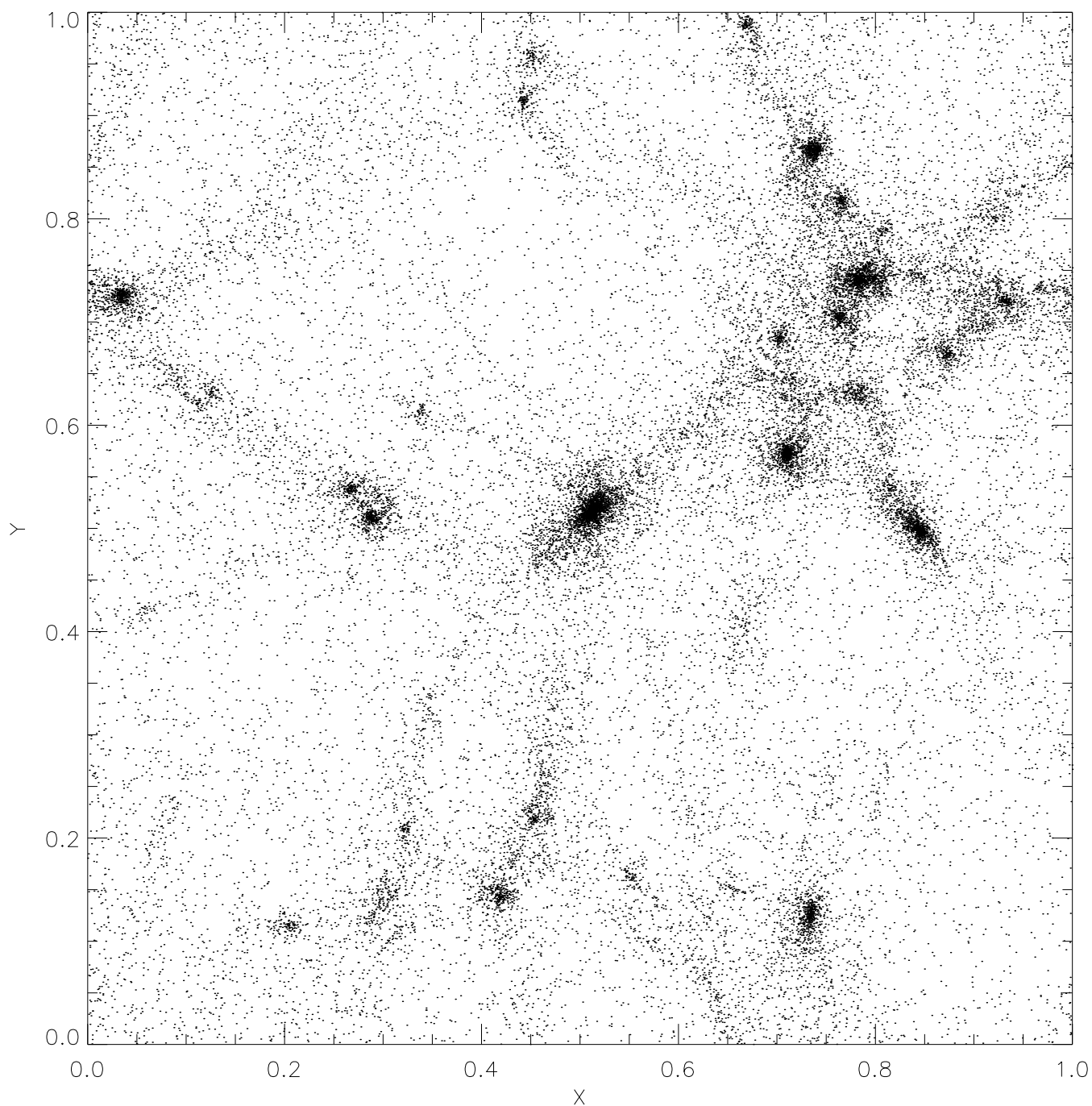


Fig. 10. Result of a pure N-body unstructured mesh simulation with mesh refinement. All the 32^3 particles are projected in the X-Y plane. The raw mesh is a 32^3 uniform mesh. Refinement is done by a mass criterion $m_c = 5 m_i$, where m_i is the mass of each particle.

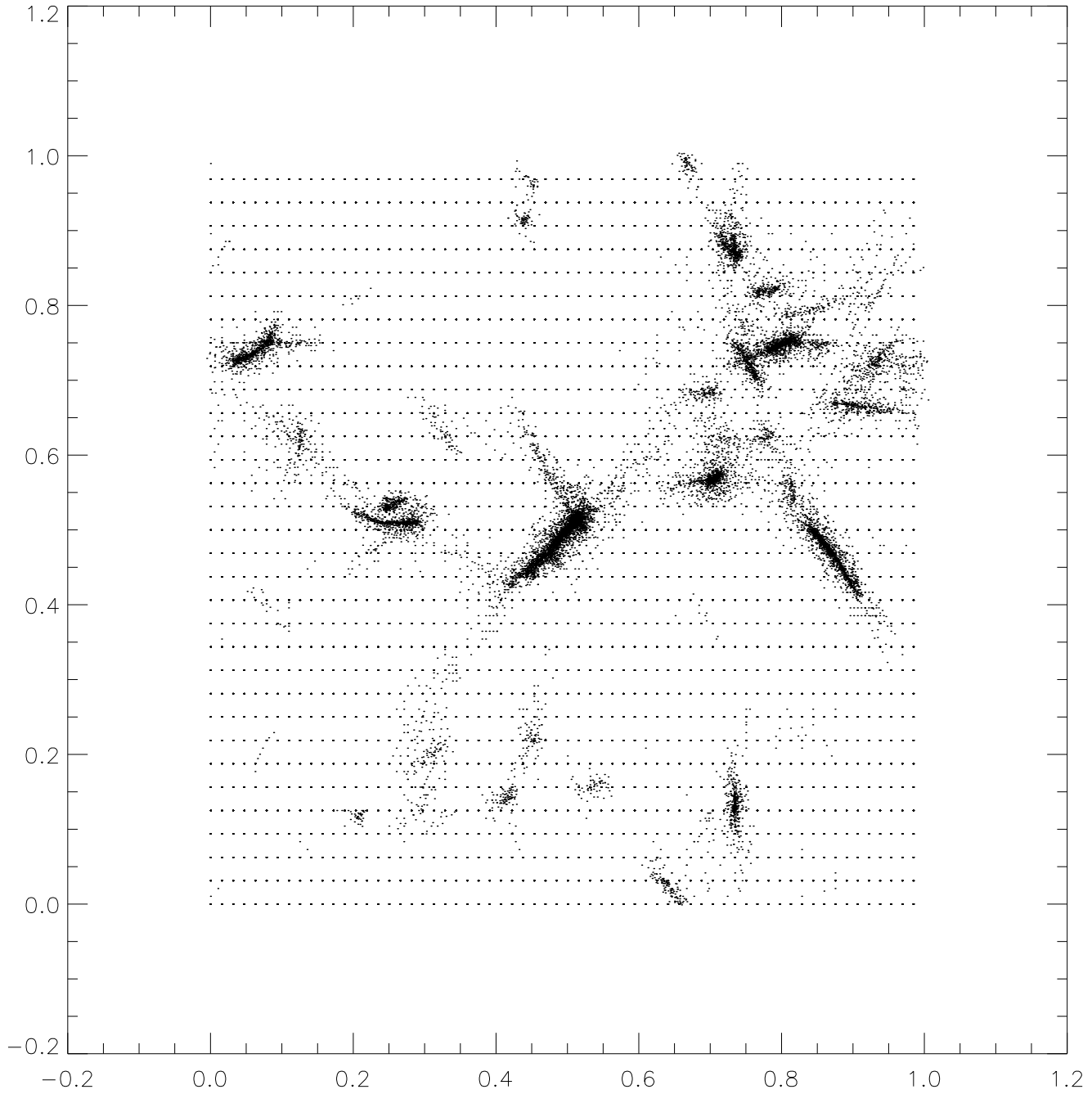


Fig. 11. Distribution of the mesh nodes projected to the X-Y plane. The particle distribution of this simulation is shown in Figure 10.

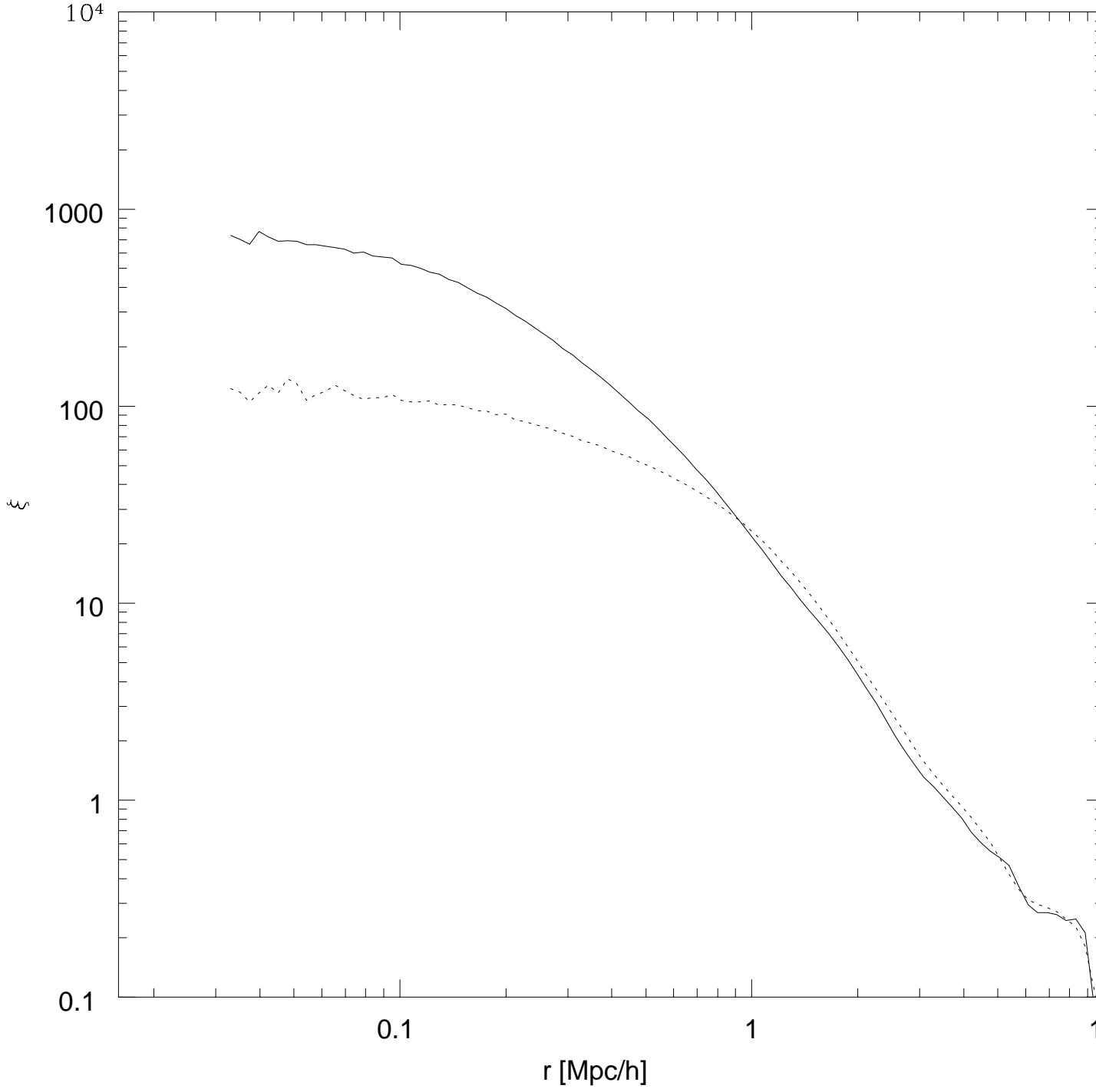


Fig. 12. The two-point correlation function $\xi(r)$ for two dark matter only simulations. The solid line is for the simulation with mesh refinement, and the dashed line is without mesh refinement. In both simulations, 32^3 particles are used on a raw mesh of 32^3 nodes. The cell size for the raw mesh is $1 \text{ Mpc}/h$.

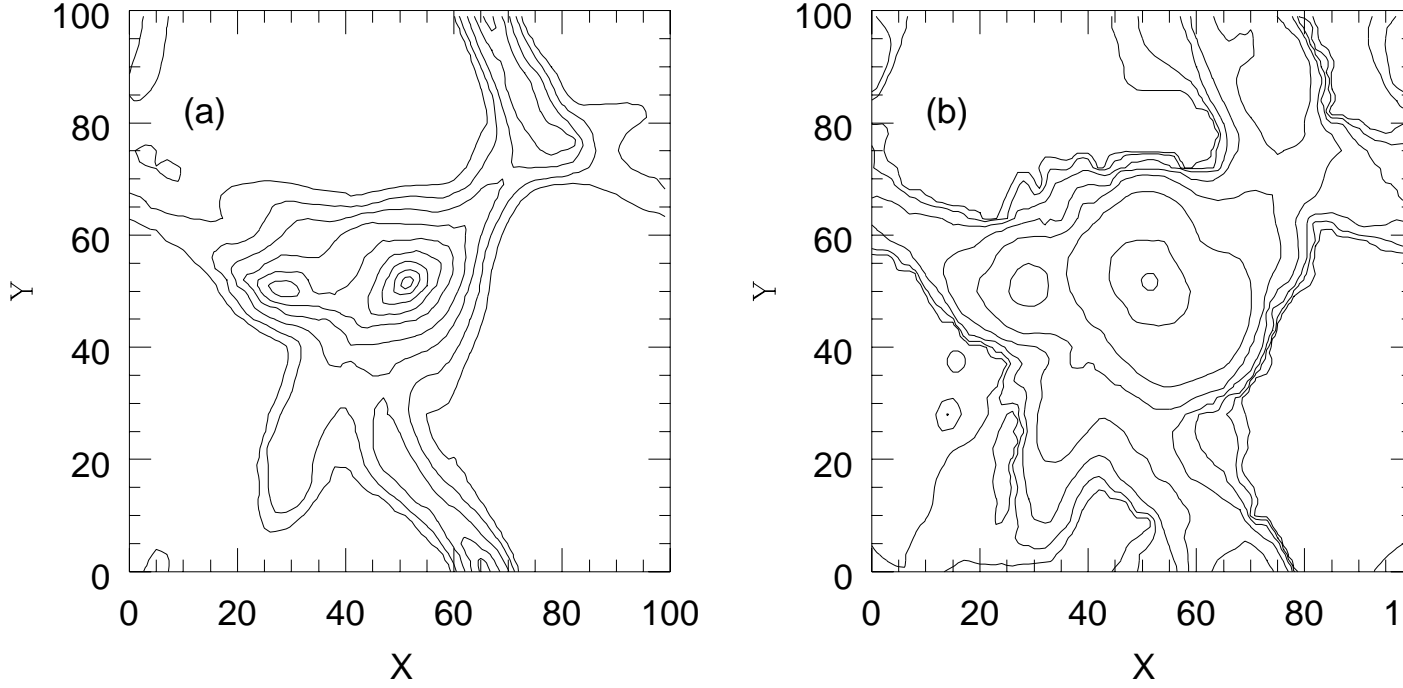


Fig. 13. Panel (a) shows the density contours of a slice in the simulation. The contour levels are $\rho = \langle \rho \rangle = 10^{k+4}$ with $k = 0, 1, \dots$. Panel (b) shows the temperature contours of the same slice with contour levels $T = 10^{5+k+2} \text{K}$ with $k = 0, 1, 2, \dots$.

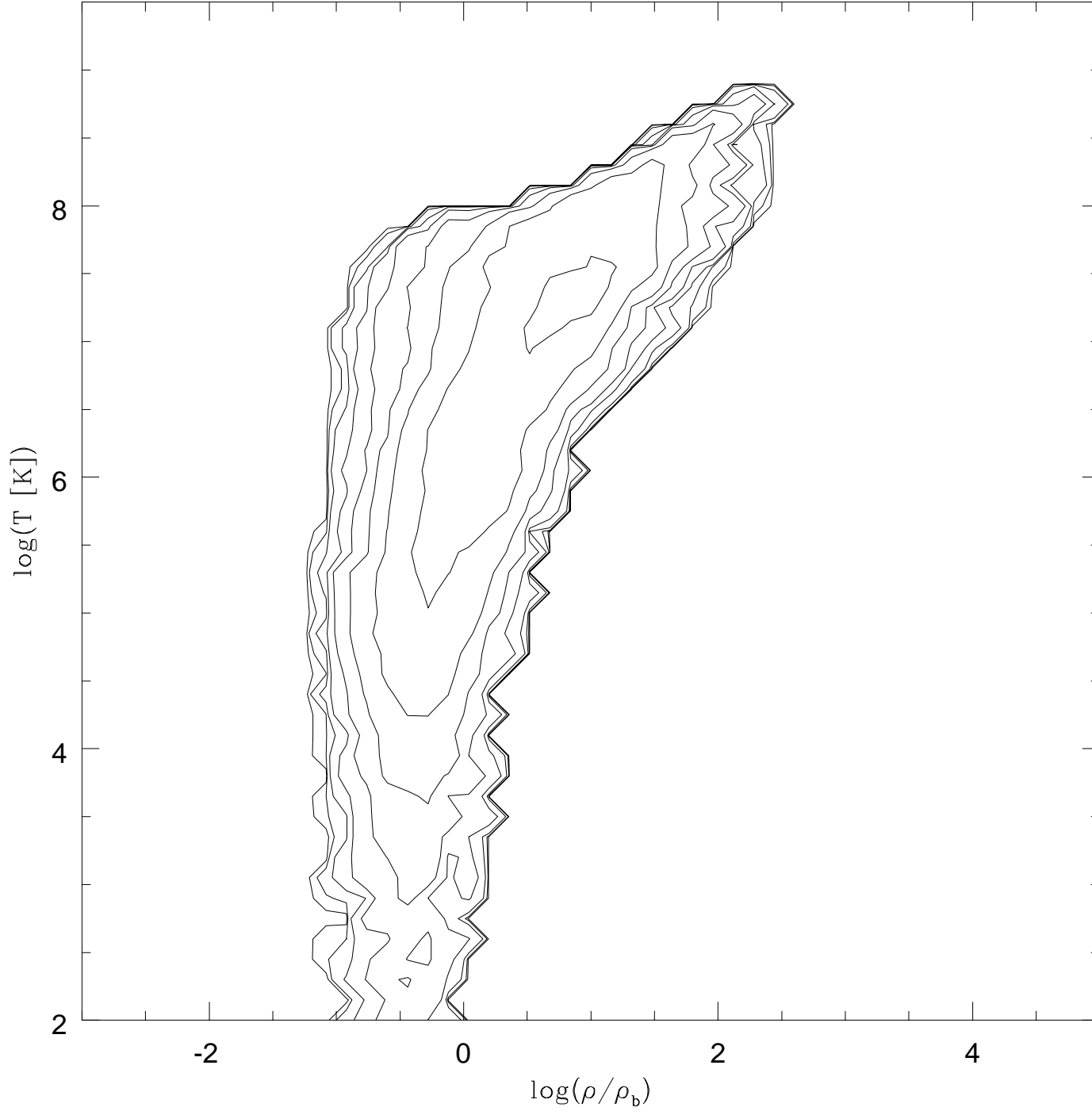


Fig. 14. Mass contour of gas at different density and temperature. The total mass in the box is 1. The contour levels are in 10^{i-2} , $i = 4; \dots; 8$, assumed to be 1.